



# A composite $^{10}\text{Be}$ , IR-50 and $^{14}\text{C}$ chronology of the pre-Last Glacial Maximum (LGM) full ice extent of the western Patagonian Ice Sheet on the Isla de Chiloé, south Chile ( $42^\circ\text{S}$ )

Juan-Luis García<sup>1</sup>, Christopher Lüthgens<sup>2</sup>, Rodrigo M. Vega<sup>3</sup>, Ángel Rodés<sup>4</sup>, Andrew S. Hein<sup>5</sup>, and Steven A. Binnie<sup>6</sup>

<sup>1</sup>Instituto de Geografía, Facultad de Historia, Geografía y Ciencia Política, Pontificia Universidad Católica de Chile, Avenida Vicuña Mackenna 4860, Macul, Santiago, 782-0436, Chile

<sup>2</sup>Institute for Applied Geology, University of Natural Resources and Life Sciences (BOKU), Vienna, 1190, Austria

<sup>3</sup>Instituto de Ciencias de la Tierra, Facultad de Ciencias, Universidad Austral de Chile, Valdivia, 5091000, Chile

<sup>4</sup>Scottish Universities Environmental Research Centre, Rankine Avenue, Scottish Enterprise Technology Park, East Kilbride, G75 0QF, UK

<sup>5</sup>School of GeoSciences, University of Edinburgh, Edinburgh, Scotland, EH8 9XP, UK

<sup>6</sup>Institut für Geologie und Mineralogie, Universität zu Köln, Zùlpicher Str. 49b, Gebäude 310, 50674, Köln, Germany

**Correspondence:** Juan-Luis García ([jgarciab@uc.cl](mailto:jgarciab@uc.cl))

**Relevant dates:** Received: 11 August 2020 – Revised: 5 February 2021 – Accepted: 23 March 2021 –  
Published: 20 May 2021

**How to cite:** García, J.-L., Lüthgens, C., Vega, R. M., Rodés, Á., Hein, A. S., and Binnie, S. A.: A composite  $^{10}\text{Be}$ , IR-50 and  $^{14}\text{C}$  chronology of the pre-Last Glacial Maximum (LGM) full ice extent of the western Patagonian Ice Sheet on the Isla de Chiloé, south Chile ( $42^\circ\text{S}$ ), E&G Quaternary Sci. J., 70, 105–128, <https://doi.org/10.5194/egqsj-70-105-2021>, 2021.

**Abstract:** Unanswered questions about the glacier and climate history preceding the global Last Glacial Maximum (LGM) in the southern temperate latitudes remain. The Marine Isotope Stage (MIS) 3 is normally understood as a global interstadial period; nonetheless its climate was punctuated by conspicuous variability, and its signature has not been resolved beyond the polar realms. In this paper, we compile a  $^{10}\text{Be}$  depth profile, single grain infrared (IR) stimulated luminescence dating and  $^{14}\text{C}$  samples to derive a new glacier record for the principal outwash plain complex, deposited by the western Patagonian Ice Sheet (PIS) during the last glacial period (Llanquihue Glaciation) on the Isla de Chiloé, southern Chile ( $42^\circ\text{S}$ ). In this region, the Golfo de Corcovado Ice Lobe left a distinct geomorphic and stratigraphic imprint, suitable for reconstructing former ice dynamics and timing of past climate change. Our data indicate that maximum glaciation occurred by  $57.8 \pm 4.7$  ka without reaching the Pacific Ocean coast. Ice readvanced and buttressed against the eastern side of the Cordillera de la Costa again by  $26.0 \pm 2.9$  ka. Our data further support the notion of a large ice extent during parts of the MIS 3 in Patagonia and New Zealand but appear to contradict near contemporaneous interstadial evidence in the southern midlatitudes, including Chiloé. We propose that the PIS expanded to its full-glacial Llanquihue moraines, recording a rapid response of southern mountain glaciers to the millennial-scale climate stadials that punctuated the MIS 3 at the poles and elsewhere.

**Kurzfassung:**

Hinsichtlich der Glazial- und Klimageschichte vor dem letztglazialen Maximum (LGM) in den temperierten Breiten der Südhemisphäre sind derzeit vielen Fragen noch unbeantwortet. Das Marine Isotopenstadium (MIS) 3 wird gemeinhin als globale interstadiale Phase verstanden, die jedoch durch phasenweise starke Variabilität gekennzeichnet war, deren Verlauf jenseits der Polargebiete jedoch noch nicht aufgelöst werden konnte. In dieser Studie werden ein  $^{10}\text{Be}$  Tiefenprofil, Datierungsergebnisse von Einzelkorn-Lumineszenz-Messungen mittels infraroter (IR) Stimulation und Alter von  $^{14}\text{C}$  Datierungen kompiliert, um für den Haupt-Sander-Komplex, der vom westlichen Patagonischen Eisschild (PIS) während des letzten Glazials (Llanquihue Vereisung) auf der Isla de Chiloé (südliches Chile,  $42^\circ\text{S}$ ) aufgebaut wurde, eine neue Vereisungschronologie aufzubauen. In dieser Region ermöglichen die deutliche geomorphologische und stratigraphische Prägung durch den Golfo de Corcovado Lobos die Rekonstruktion von vergangener Eisdynamik und der Zeitstellung klimatischer Veränderungen. Unsere Ergebnisse besagen, dass sich die maximale Eisausdehnung um  $57.8 \pm 4.7\text{ ka}$  einstellte. Der Pazifik wurde hierbei nicht erreicht. Ein erneuter Eisvorstoß entlang der östlichen Flanke der Cordillera de la Costa kann um  $26.0 \pm 2.9\text{ ka}$  nachgewiesen werden. Unsere Daten unterstützen damit die Auffassung von der Existenz großer Eisausdehnungen im MIS 3 in Patagonien und Neuseeland, aber scheinen jedoch zeitgleiche Erkenntnisse aus benachbarten Regionen zum Interstadial der südlichen Mittelbreiten, einschließlich Chiloé, zu konterkarieren. Wir erklären die Ausdehnung des PIS zu den Llanquihue Endmoränen als schnelle, kurzfristige Reaktion südlicher Gebirgsgletscher auf kurze (tausendjährige Zeitskala) stadiale Phasen innerhalb des MIS 3 Interstadials, die bereits an den Polen und andernorts nachgewiesen werden konnten.

**1 Introduction**

We lack thorough knowledge on the timing of the local Last Glacial Maximum (LGM) for the Southern Hemisphere mountain glaciers because the dating of their terminal moraines and associated outwash plains has remained spatially variable. Understanding the glacial fluctuations throughout this recent glacial period (e.g., Marine Isotope Stage, MIS, 4 through MIS 2) is a prerequisite for uncovering the cause and climate mechanisms driving southern glaciation and the interhemispheric linkages of climate change (Denton et al., 1999a). Similarly, defining the ice extent is key for understanding the magnitude of the last glaciation in the southern Andes (e.g., the LGM) and thereby the main paleoclimatological, geomorphological and paleoecological implications. In addition to MIS 2, new records indicate extensive glaciers during MIS 3, MIS 4 and late MIS 5 in southern Patagonia and New Zealand, but uncertainty remains as to whether this is a common feature of southern midlatitude glacial history (Schaefer et al., 2015; Williams et al., 2015; Darvill et al., 2015; Kelley et al., 2014; García et al., 2018; Davies et al., 2020; Mendelová et al., 2020; Shulmeister et al., 2010). Moreover, the MIS 3 is normally referred to as a global interstadial period when southern conifer forest expanded to ice-free low-land areas, but glaciers are also known to have advanced in southern Chile and New Zealand by this time (Villagrán et al., 2004; Kelley et al., 2014; Darvill et al., 2015; García et al., 2018). Despite the fact that paleoclimate records are well-resolved in the polar regions, main knowledge gaps remain for the terrestrial southern midlatitudes before the global LGM time frame.

Here, we present new geochronological data from a  $^{10}\text{Be}$  depth profile, infrared (IR) stimulated luminescence dating using single grains of potassium-rich feldspar (Fs) and  $^{14}\text{C}$  samples of the two Cucao main outwash terraces (Cucao\_T1 and Cucao\_T2) on the Isla de Chiloé, south Chile ( $42^\circ\text{S}$ ) (Figs. 1 and 2). These extensive outwash plains were deposited by the Golfo de Corcovado Ice Lobe of the northwest Patagonian Ice Sheet (PIS) during the Llanquihue Glaciation (i.e., the last glacial period). Together with Cucao\_T1 and Cucao\_T2, multiple pairs of outwash terraces occupying similar morphostratigraphic positions occur on the lee side of the Cordillera de la Costa and represent the full glacial extent in Chiloé (Fig. 1). These outwash terraces can be traced to ice-contact slopes on the east side of the Cordillera de la Costa as they have been previously mapped (García, 2012). Thus, the dating of the Cucao\_T1 and Cucao\_T2 terraces can help reconstruct the LGM of the PIS and the overall glacier and climate history that preceded the well-known LGM (MIS 2) in the region (Mercer, 1976; Laugénie, 1982; Porter, 1981; Bentley, 1997; Denton et al., 1999b). Our record builds on previous work in the Chilean Lake District (CLD) by dating glacially derived sediments that can be directly related to a landform, thereby determining the extent of glacier advances during the last glacial period. Dating landforms beyond the  $^{14}\text{C}$  range in Chiloé is challenging. Exposed bedrock and boulders resting on glacial landforms are very rare, rendering commonly used cosmogenic nuclide exposure-dating techniques impractical. Here, we constrain the timing of maximum ice extent, as recorded by glacial landform and deposit associations, by applying a composite geochronologic approach.

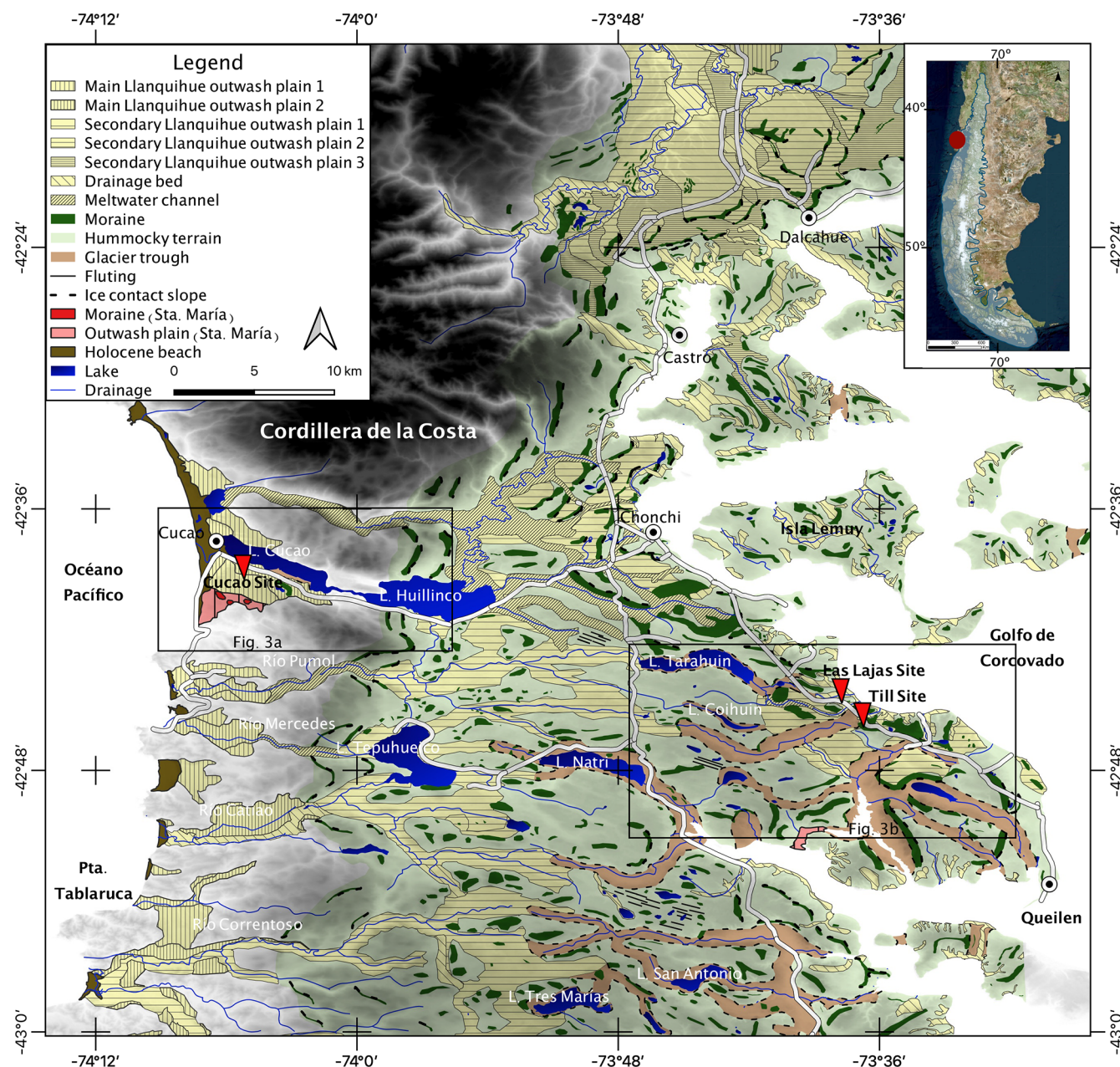


**Figure 1.** The Cucao site in the context of the former Patagonian Ice Sheet (PIS) and the glacial geomorphologic setting of the Archipiélago de Chiloé. The red circle in the inset indicates the location of the study area in the northwest sector of the former PIS (outlined). Note the location of stratigraphic sites presented in this study and mentioned in the text. For the sake of space, the Cucao site in the map indicates the geographic location of all seven sites studied within this sector. For more details, see Figs. 2 and 3a. Geomorphic map modified from García (2012). Base map is the 30 × 30 Shuttle Radar Topography Mission (SRTM) extracted from NASA JPL (2013).

### 1.1 The Llanquihue Glaciation

The Llanquihue Glaciation is the local name for the last glacial period in southern Chile, particularly the CLD and the Archipiélago de Chiloé (39–42° S) (Heusser and Flint, 1977; Porter, 1981; Laugénie, 1982; Denton et al., 1999b; García, 2012). Glacial landforms and sediments from the last ice period display excellent preservation and limited weath-

ering, respectively. García (2012) suggested that a mountain style of glaciation characterized the CLD. Different subglacial landforms, including drumlinoid and fluting landforms, within extensive, mostly uninterrupted ice-marginal positions denote rather an ice-sheet style of glaciation to the south on the Isla Grande de Chiloé. For instance, a west–east transect across the moraine field in the CLD and northern Isla de Chiloé reveals a stepwise topography punctuated by dis-



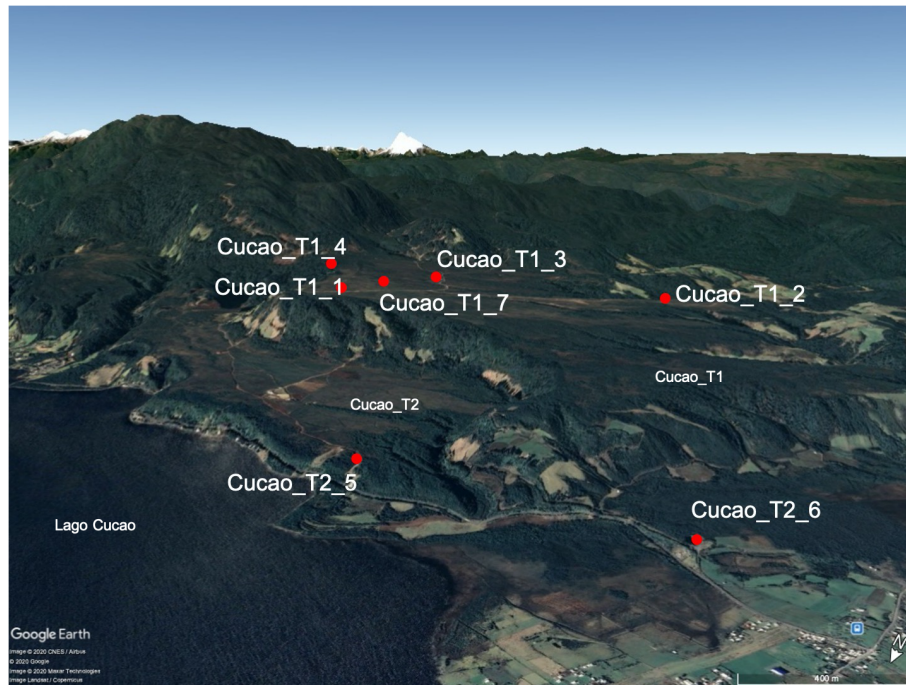


**Figure 2.** Oblique view of the Cucao\_T1 and Cucao\_T2 outwash terraces and the studied Cucao sites. All Cucao sites occur in these terraces on the western side of the Cordillera de la Costa. View is to the south-southeast. Ice flow from the upper left. Base image from © Google Earth.

tinct ice-contact slopes, composite moraines, and associated main and subsidiary outwash plains (Andersen et al., 1999; Denton et al., 1999b). To the south of Dalcahue, a double moraine and ice-contact slope preserved on the eastern slope of the Cordillera de la Costa represents the outermost extents of the ice during the Llanquihue Glaciation in Chiloé (García, 2012). Beyond this ice-marginal position, meltwater channels carved the bedrock and fed outwash terraces on the Pacific mountain side. Accordingly, the Huillinco and Cucao lakes (Fig. 1), which interrupt the continuity of the Cordillera de la Costa, likely allowed the ice to trespass towards the west. Otherwise, the ice buttressed on the eastern mountain side. It has been suggested that the outer Llanquihue landforms (i.e., the early Llanquihue time) were deposited during the Marine Isotope Stage (MIS) 4 (e.g., Denton et al., 1999b; García, 2012). This conclusion is based on the landform and sediment preservation, together with the infinite uncalibrated age  $> 50\,000$   $^{14}\text{C}$  yr BP, of the Taiquemó record (Heusser et al., 1999), which is located inboard from the early Llanquihue moraine in northern Chiloé. In addition, sea surface temperatures (SSTs) offshore northern Chiloé uncover the coldest glacial conditions in the ocean during MIS 4 (Kaiser et al., 2005). Nonetheless, the early Llanquihue landforms have remained mostly undated, which in turn is the main research focus of this paper.

The MIS 3 in Chiloé and the CLD have been regarded as an interstadial period based on pollen and sub-fossil-tree records constrained by finite and mostly infinite  $^{14}\text{C}$  ages

(e.g., Heusser et al., 1999; Roig et al., 2001; Villagrán et al., 2004). At this time conifer forests dominated, indicating a relatively mild and humid climate (Villagrán et al., 2004). However, high variability between arboreal and herbaceous vegetation also occurred, which suggests climate instability through the MIS 3 (Heusser et al., 1999). The same conclusion can be extracted from the SST record offshore Chiloé (Kaiser et al., 2005).

For MIS 2, Denton et al. (1999b) determined the timing of at least four glacial advances in the CLD and northern Isla Grande de Chiloé, which significantly added to the previous work in the region (Mercer, 1976; Porter, 1981; Bentley, 1997). From their radiocarbon chronology, Denton et al. (1999b) defined the timing of the LGM to between 34.3 and 18.0 cal kyr BP. In central Chiloé, a glacial advance occurred before 28 cal kyr BP and at 26.0 cal kyr BP (García, 2012). The regional equilibrium line altitude (ELA) was depressed  $\sim 1000$  m relative to the present (Porter, 1981; Hubbard et al., 2005). This corresponds to an estimated drop of 6 to 8 °C in mean summer temperature and mean annual precipitation  $\sim 2000$  mm yr $^{-1}$  greater than present (Heusser et al., 1996, 1999; Villagrán, 1988, 1990). The end of the LGM was marked by abrupt glacial retreat after 18 cal kyr BP, both in the CLD and Chiloé (Lowell et al., 1995; Denton et al., 1999b).



## 1.2 Regional setting

The Archipiélago de Chiloé is separated from the mainland by the Golfo de Ancud and Golfo de Corcovado, where intervening seawaters can reach > 400 m but mostly less than 200 m depth. The western Patagonian Andes facing Chiloé reach higher elevations and contain a significantly larger number of glaciers than the CLD to the north, with ice caps on peaks > 2000 m a.s.l. (Barcaza et al., 2017).

South of 40° S, the southwesterly circulation is present throughout the year (Garreaud et al., 2009). This zonal wind extends through the whole troposphere and occurs as a mostly symmetric belt in the southern midlatitudes. The westerly wind belt in the Pacific occurs in a zone constrained mainly by the effect of the subtropical anticyclone and the polar front, and today it produces a precipitation peak at 45–47° S (Miller, 1976). Seasonal expansion (winter) and contraction (summer) of the westerly wind belt and associated storm circulation govern the climate along extratropical Chile. Chiloé intersects the northern margin of the westerly wind belt, which results in humid winters (> 1000 mm of precipitation between May–August in Castro; Luebert and Plissock, 2006) and rather dry summers due to the blocking effect of the Pacific high-pressure cell (Miller, 1976; Garreaud et al., 2009). In South America, precipitation to the west of the southern Andes chain is positively correlated to the westerly wind strength, while the opposite occurs to the east of the Andes, where a rain shadow dominates (Garreaud, 2007). Mean air temperatures in Chiloé fluctuate from about 8 °C in winter to 14 °C in summer, reflecting a west-coast, southern-midlatitude maritime climate regime. Nonetheless, freezing temperatures can occur late in the autumn. Climate variability at decadal to interdecadal timescales is affected by pressure anomalies in the Antarctic and the southern midlatitudes (the Southern Annular Mode, SAM) thus controlling the strength and position of the westerly wind, precipitation yields and surface air temperatures south of 40° S (Garreaud et al., 2009, 2013).

Offshore Chiloé, the north branch of the Antarctic Circumpolar Current (ACC) shows the steepest thermal latitudinal gradient (Kaiser et al., 2005). This abrupt change in SST temperatures is linked with the southwesterly wind's northern boundary (Strub et al., 1998). Just south of Chiloé, the ACC separates into the northward Humboldt Current and the southward Cape Horn Current (Lamy et al., 2015). The Humboldt Current transports subantarctic surface waters of the ACC along the Chilean coast with mean annual SST offshore Chiloé reaching ~ 13 °C (Kaiser et al., 2005). The ocean and atmosphere circulation are intimately linked and experienced large changes during the LGM affecting the PIS fluctuations (Lamy et al., 2015).

## 2 Methods

For studying the Cucao terraces, we selected a total of seven sites, including sediment pits and road sediment sections in both Cucao\_T1 and Cucao\_T2 (Figs. 2 and 3a). The number and distribution of sites help us to constrain the age of these glaciofluvial landforms. Most of sites occur on top of the glaciofluvial plains (sites Cucao\_T1\_1–3 and \_7) except for Site Cucao\_T1\_4, Site Cucao\_T2\_5 and Site Cucao\_T2\_6, which occur by the edge of the terraces. We also study a stratigraphic section in eastern Chiloé (the Till site) which, together with the Las Lajas site (García, 2012), adds context for interpreting Cucao data.

### 2.1 Mapping and sedimentology

The mapping produced here builds on previous work in the area (Heusser and Flint, 1977; Andersen et al., 1999; García, 2012). We took advantage of new sediment exposures in the study area to produce more detailed observations of sediments and landforms during multiple field campaigns developed between 2016–2019. For better description and interpretation of the geomorphology, we analyzed SRTM\_GL1 (Nasa JPL, 2013) and reexamined aerial photographs of the study area. Sediment analysis includes modified facies codes based on Miall (1985, 2006), Eyles et al. (1983), and Maizels (1993). We applied traditional sedimentology and geomorphology techniques in order to describe the glacial and proglacial environments as a basis for our dating approach.

### 2.2 Geochronology

#### 2.2.1 Radiocarbon

We radiocarbon dated both bulk organic sediment and wood samples. We targeted in situ organic stratigraphic units or reworked organic mud clasts embedded in outwash sediments. The interpretation of our <sup>14</sup>C data varied depending on the setting, as described in the results section. All <sup>14</sup>C ages in this paper are presented as the mean ± uncertainty of the reported 2σ range except where indicated. The ages were calculated using CALIB REV7.1 online web calculator (Stuiver et al., 2020) and the Southern Hemisphere <sup>14</sup>C calibration curve (Hogg et al., 2013). The <sup>14</sup>C calibrated ages include > 0.9 probability within the 2σ range. This is true for all data presented except sample CUCAOT1-1803\_III (> 0.7).

#### 2.2.2 The <sup>10</sup>Be depth profile

We selected a stratigraphic column at the Site Cucao\_T1\_3 section with an accessible sediment depth reaching ~ 300 cm (Fig. 4). This site is suitable for building a <sup>10</sup>Be depth profile as the sediments appear to have been deposited on top of each other in a continuous and rapid fashion (Hein et al., 2009; Darvill et al., 2015). Nonetheless, the sediment section where

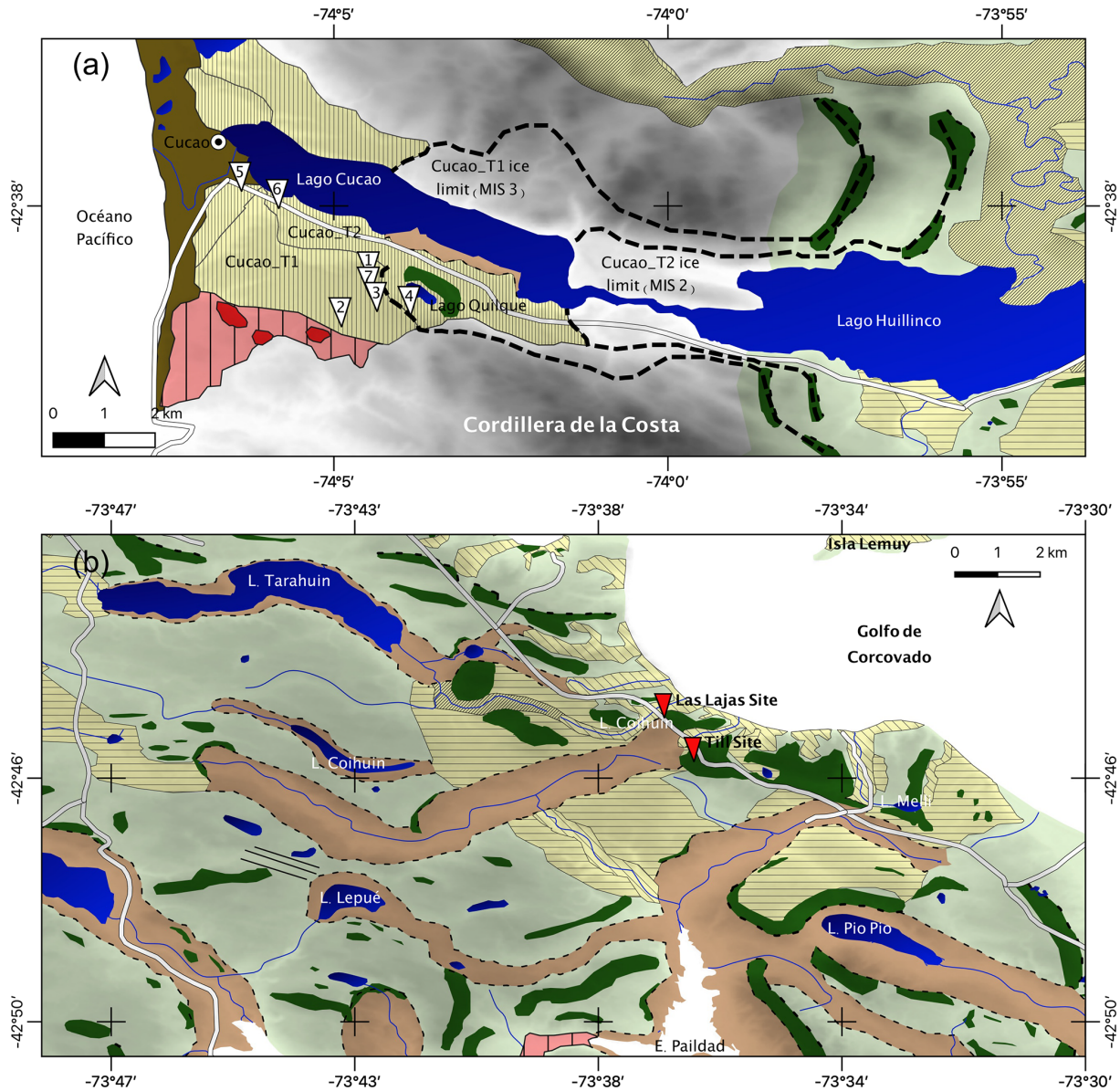


**Figure 3.** Geomorphologic maps showing the morphostratigraphic relationships between the Cucao sites (a) and Las Lajas and Till sites (b). Also shown in (a) are the inferred ice limits (dashed lines) associated with the deposition of Cucao\_T1 and Cucao\_T2 terraces. Both of these terraces are separated by a distinct fluvial scarp that in part could have been formed as an ice contact slope (see text for discussion). Legend codes in Fig. 1.

the  $^{10}\text{Be}$  profile was sampled includes a top organic soil (upper 35–20 cm) that overlies outwash sediment, and therefore no surface cobbles were found for dating. An iron-rich layer occurs at 70 cm below the original surface within the outwash sediments. Above this iron layer, the sediment can appear oxidized, which is not the case towards the bottom of the sediment section.

The most critical parameter to model how the  $^{10}\text{Be}$  accumulates underground is the evolution of the surface erosion/accretion affecting the depth of the quartz grains (samples) through time. This is because the cosmogenic  $^{10}\text{Be}$  pro-

duction rate decreases exponentially with cumulative mass depth (expressed in  $\text{g cm}^{-2}$ ). To relate cumulative mass depth to the sampling depth within a sediment layer requires an estimate of the overlying bulk soil density. For our model, we considered the outwash sediment bulk density to be between 1.9 and 2.2  $\text{g cm}^{-3}$ , based on the visual estimation of porosity between 20 % and 30 %, with variable moisture between 30 % and 60 %, and for a grain density of 2.6  $\text{g cm}^{-3}$ . This density range coincides with the densities of gravel-bearing unconsolidated materials listed in Manger (1963). We include the top organic soil (see Sect. 3) in this range. For



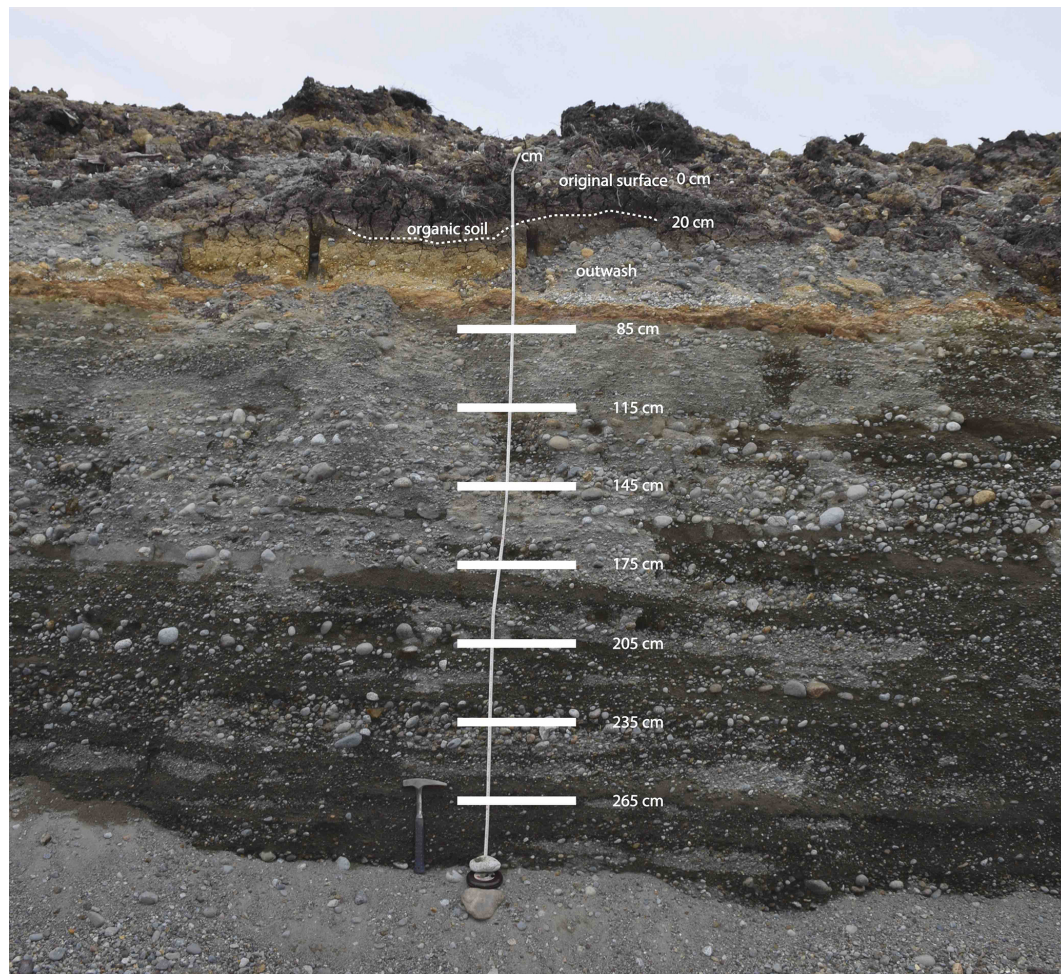


**Figure 4.** Cucao\_T1  $^{10}\text{Be}$  depth profile produced in Cucao\_T1\_3 site. Note the original surface (underlying not in situ mixed soil remains) and the in situ organic soil and outwash sediment surface contact (dashed white line). Solid white rectangles indicate  $^{10}\text{Be}$  sample locations with associated depths.

testing our  $^{10}\text{Be}$  profile models for Cucao\_T1\_terrace,  $^{10}\text{Be}$  concentrations produced in situ were measured in quartz obtained from seven amalgamated sand and pebble sample layers. We collected about 3 cm thick layers each 30 cm between 85–265 cm depth (Fig. 4). Model concentrations were calculated at the center of the sampling layers. We did not sample the top 50 cm of the outwash to avoid vertical sediment mixing due to potential root development near the surface.

Sediment  $^{10}\text{Be}$  sample preparation as an accelerator mass spectrometry (AMS) target was done at University of Edinburgh's cosmogenic nuclide laboratory. The  $^{10}\text{Be}$  was selectively extracted from 20 to 26 g of pure quartz following standard methods (Bierman et al., 2002; Kohl and Nishizumi, 1992). The samples and the process blanks ( $n = 1$ ) were spiked with  $\sim 0.25 \text{ mg } ^9\text{Be}$  carrier (Scharlau Be carrier,  $1000 \text{ mg L}^{-1}$ , density  $1.02 \text{ g mL}^{-1}$ ). The samples were prepared as BeO targets for AMS analysis following procedures detailed by Hein (2009). Measurements of  $^{10}\text{Be}/^9\text{Be}$  ratios

were undertaken at CologneAMS (Dewald et al., 2013), normalized to the revised standard values reported by Nishizumi et al. (2007). Blank  $^{10}\text{Be}/^9\text{Be}$  ratios ranged between 1 % and 5 % of sample  $^{10}\text{Be}/^9\text{Be}$  ratios. Table 1 shows other  $^{10}\text{Be}$  data from this study.

The  $^{10}\text{Be}$  accumulation was modeled following the formulae of Lal (1991). The time was discretized to accommodate the change in the samples' depths due to the accumulation of the overlaying organic sediment. Monte-Carlo simulations (as in Hidy et al., 2010) were used to find the fitting values of the following free parameters: (1) the age of the outwash sedimentary package, (2) the age of the overlaying organic soil and (3) the initial  $^{10}\text{Be}$  accumulated before the outwash deposition, which is considered to be constant along the outwash profile. Random values of bulk density between  $1.9$  and  $2.2 \text{ g cm}^{-3}$  were considered for the entire profile. Probabilities corresponding to the chi-square values of the individual models were used to calculate the probabil-



**Table 1.** The  $^{10}\text{Be}$  data for depth profiles in the Cucao\_T1 terrace.

Sample ID	Latitude (dd)	Longitude (dd)	Altitude (m a.s.l.)	Depth (cm)	Thickness (cm) <sup>a</sup>	Quartz mass (g)	$^{10}\text{Be}$ measured ( $10^4 \text{ atom g}^{-1}$ ) ( $\pm 1\sigma$ ) <sup>b</sup>
Cucao_115	42.6659	74.0777	112	85	3.0	23.5264	$12.144 \pm 1.393$
Cucao_145				115	3.0	22.2588	$8.376 \pm 1.086$
Cucao_175				145	3.0	24.3108	$6.747 \pm 0.404$
Cucao_205				175	3.0	22.3157	$6.301 \pm 0.753$
Cucao_235				205	3.0	22.466	$4.302 \pm 0.734$
Cucao_265				235	3.0	26.6511	$2.384 \pm 0.209$
Cucao_295				265	3.0	24.8943	$4.125 \pm 0.869$

<sup>a</sup> This is the approximate thickness of the layer of amalgamated sediment collected at each specified depth. <sup>b</sup> Nuclide concentrations are normalized to revised  $^{10}\text{Be}$  standards and half-life ( $1.36 \pm 0.07 \text{ Myr}$ ) of Nishiizumi et al. (2007) and include propagated AMS sample and lab-blank uncertainty and 2 % carrier mass uncertainty. Quartz density is  $2.7 \text{ g cm}^{-3}$ . Topographic shielding at the profile site is negligible (0.9999).

ity density distributions of the parameters. The method described in Rodés et al. (2011) was used to select the models fitting the data within a  $1\sigma$  confidence level. We initially modeled the effect of gradual (linear with time) accretion of the organic sediment. The Be-10 profiles under the organic sediment generated by these models were identical to those generated for instantaneous deposition of the organic sediment layer at an intermediate time (between the outwash formation and today). Therefore, the formation age of the organic sediment was considered an unknown variable in the models presented here in order to simulate all extreme scenarios. As the timing of the process that produced the organic soil is unknown, two scenarios were considered. Scenario “a” does not consider the shielding produced by the organic layer, as would be appropriate if the latter was formed recently or for a limited time span. The models fitting this scenario provide a minimum estimate for the outwash deposition age as they consider the conditions that maximize the  $^{10}\text{Be}$  production rate at the sample depths. Scenario “b” considers that the organic layer could be deposited anytime between the outwash deposition and today. The models fitting this scenario should cover all the possible and the less restrictive age ranges for the deposition of the Cucao\_T1 outwash. The models assume no surface erosion occurred after outwash deposition as negligible erosion rates are expected in abandoned outwash plains in relatively short time spans (i.e., the last glacial period) (Hein et al., 2009). We used  $^{10}\text{Be}$  production rates of 4.0678, 0.0383 and  $0.0404 \text{ atoms g}^{-1}$  and attenuation lengths of 160, 2481 and  $1349 \text{ g cm}^{-2}$ , for spallation and fast and stopping muons, respectively. This is in agreement with the average production rate corresponding to the Lago Argentino calibration data in Patagonia (Kaplan et al., 2011) scaled according to the online calculators formerly known as the CRONUS-Earth online calculators v.3 (Balco et al., 2008) for the last  $\sim 100 \text{ kyr}$  and using the scaling scheme of LSDn (Lifton et al., 2014). The LSDn is based on models derived from theory and includes estimates for a

time-dependent magnetic field (Lifton et al., 2014). Although the selection of this scaling scheme does not affect our conclusions, we chose to use the Lago Argentino calibration and LSDn scaling scheme in order to facilitate the direct comparison of our ages with other published cosmogenic ages in Patagonia (e.g., Davies et al., 2020).

### 2.2.3 Luminescence dating approach

We collected luminescence samples by driving opaque tubes into soft sand sediments within the outwash deposits of Cucao\_T1 (sites \_1, \_2 and \_3; four samples) and Cucao\_T2 (sites \_5 and \_6; two samples). Luminescence dating techniques in general allow for the determination of depositional ages of sediments by calculating the point in time when the sediments were last exposed to daylight (during transport) and subsequently shielded from daylight (deposition). The build-up of a latent luminescence signal in quartz- and potassium-rich feldspar minerals is time dependent and induced by naturally occurring radiation (cosmic radiation and ionizing radiation from naturally occurring radionuclides). Once the stored luminescence signal (termed equivalent dose) and the rate of ionizing radiation impacting the sample over time (termed the dose rate) are known, a luminescence age can be determined using the following general age equation:  $\text{age (a)} = \text{equivalent dose (Gy)} / \text{dose rate (Gy a}^{-1}\text{)}$ . For further details on luminescence dating in general, please see the following overview papers: Preusser et al. (2008), Rhodes (2011), Wintle (2008), and Smedley et al. (2016).

All sample preparation and subsequent measurements were conducted at the Vienna Laboratory for Luminescence dating (VLL) on RISØ DA20 luminescence reader systems, one of which is equipped with an 830 nm infrared laser for the stimulation of the luminescence signal of potassium-rich feldspar single grains (Bøtter-Jensen et al., 2000, 2003). All measurements were conducted using potassium-rich feldspar

because quartz from Patagonia has frequently been shown to be unsuitable for dating purposes (García et al., 2019; Duller, 2006; Glasser et al., 2006; Harrison et al., 2008; Blomdin et al., 2012; Smedley et al., 2016). All sample preparation was conducted at the VLL under subdued red light conditions to extract pure separates of potassium-rich feldspar (procedures described in detail in Lüthgens et al., 2017). Because water-lain samples in general are prone to incomplete bleaching of the luminescence signal prior to burial (insufficient exposure to daylight to reset the luminescence signal to zero), and that effect is intensified by the slow bleaching properties of potassium-rich feldspar, a single grain dating approach was adopted to detect and correct for the effects of incomplete bleaching. This methodological approach has been described in detail in García et al. (2019). All measurements were conducted using an IR-50 (infrared stimulated luminescence at a temperature of 50 °C) SAR (single aliquot regenerative) dose protocol, using the most easily bleachable K-feldspar (potassium-rich feldspar) signal (Blomdin et al., 2012). Rejection criteria ( $< 30\%$  recycling ratio,  $< 30\%$  recuperation,  $< 20\%$  test dose error) are based on results from dose recovery experiments resulting in recovery ratios in agreement with unity within error. Equivalent dose values were calculated using the bootstrapped three-parameter minimum age model (BS-MAM; Galbraith et al., 1999; Cunningham and Wallinga, 2012) with a threshold value of  $40 \pm 10\%$  for the expected overdispersion. The threshold value is based on the results from dose recovery experiments and the characteristics of the best-bleached natural sample (Figs. 5 and 6). All statistical evaluation was done using the R luminescence package of Kreutzer et al. (2012). The contents of naturally occurring radionuclides ( $^{238}\text{U}$  and  $^{232}\text{Th}$  decay chains, as well as  $^{40}\text{K}$ ) contributing to the external dose rate were determined using high-resolution, low-level gamma spectrometry (Baltic Scientific Instruments 40 % p-type HPGc detector). The dose-rate and age calculation was conducted using the software ADELE (Kulig, 2005), and all ages were corrected for fading (athermal signal loss over time; Wintle, 1973) using the approach of Huntley and Lamothe (2001) based on an average fading rate ( $g$  value of  $4.4 \pm 0.27$ ) from multiple samples determined following the approach of Auclair et al. (2003) on multi-grain aliquots, as suggested by Blomdin et al. (2012). All details concerning the experimental setup are described in García et al. (2019) and the supplement on luminescence dating in that paper. A typical dose response curve and a typical equivalent dose distribution are provided in Figs. 5 and 6 for sample VLL-0291-L. In the text, we provide the calculated IR-50 age  $\pm 1\sigma$ .

### 3 Results

Whereas the higher Cucao\_T1 outwash plain occurs at  $\sim 140$  m a.s.l., the lower Cucao\_T2 occurs at  $\sim 70$  m a.s.l. Nonetheless, both landforms show relatively high topo-

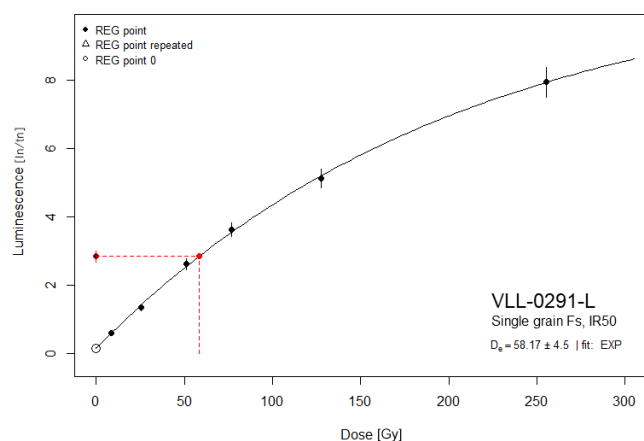


**Figure 5.** Representative dose response curve for a single K-feldspar grain of sample VLL-0291-L. Plot generated using the R luminescence package of Kreutzer et al. (2012).

graphic gradients between  $\sim 2\%$  (Cucao\_T1) and  $\sim 1.3\%$  (Cucao\_T2). Multiple outwash levels exist in between these two large outwash plains, but they are only local in extent. A main geomorphic feature is a  $\sim 30$  m tall scarp that separates Cucao\_T1 and Cucao\_T2 terraces (Fig. 3a). To the west, the Cucao\_T2 terrace is punctuated by a hummocky terrain adjacent to the T1 terrace scarp where the Quilque lake develops (Fig. 3a). The most prominent mounds are covered by dense forests, but a recently cleared inner ridge exhibits a diamictic surface with several rounded cobbles and small boulders on top partly covered by soil development. Overall, these landforms resemble a type of moraine relief surrounded by Cucao\_T2 outwash plain. The links between this moraine landform and the outwash terraces are discussed below in Sect. 4.

### 3.1 Sedimentology

We selected a total of six sites for stratigraphic sediment interpretation: Cucao\_T1 is characterized by the description of sites \_1–\_4. Cucao\_T2 is characterized based on sites \_5 and \_6 (see Figs. 2 and 3a for location and Table 2 for site details). Sedimentological description and interpretation provided here for Cucao\_T1 and Cucao\_T2 terraces allow us to discuss the type of glacial and proglacial setting during maximum glaciation in Chiloé. Site Cucao\_T1\_7 outcrops on the side of a road as a nearly 50 cm peat deposit, and therefore no sediment description was made here.

#### 3.1.1 Site Cucao\_T1\_1

The exposure consists of a series of crudely bedded, well-rounded, clast- to matrix-supported gravels (Gmg, Gcg), arranged in 0.3–0.5 m subhorizontal beds (Fig. 7a). Predominant grain size is within the pebble range, although cobble-rich bodies are common. Both upward-coarsening and upward-fining beds occur, matrix content generally

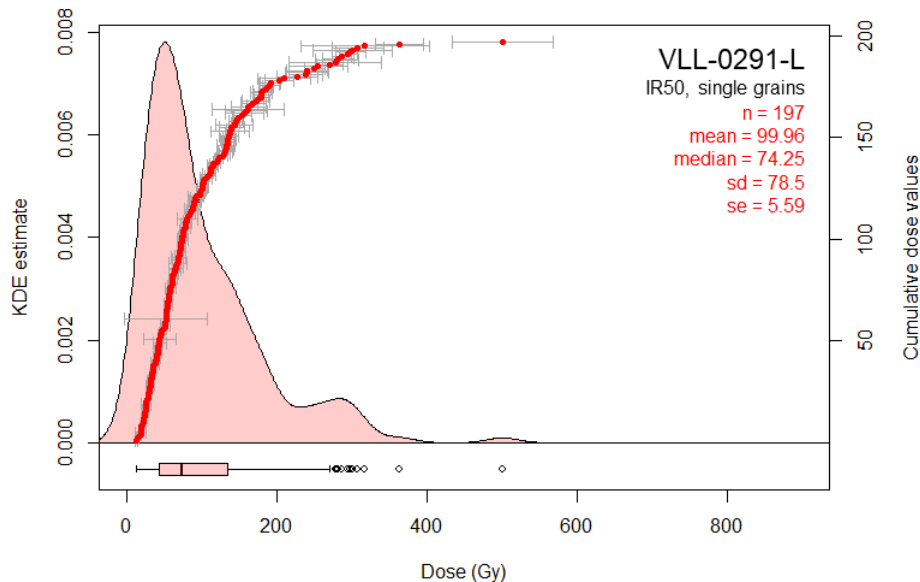


**Figure 6.** Equivalent dose distribution for sample VLL-0291-L. KDE plot (kernel density estimate) generated using the R luminescence package of Kreutzer et al. (2012). The graph shows an asymmetric, right-skewed distribution, which is typical for incompletely bleached samples.

decreasing from base to top and usually culminating in a clast-supported veneer. Beds are laterally extensive ( $> 10$  m) and mostly bounded by flat subhorizontal surfaces occasionally disrupted by shallow, narrow channel bodies filled with matrix-supported, massive, cobble-rich, imbricated gravels (Gmm, Gmi). Polymict material is predominantly of Andean origin (volcanic and intrusive rocks).

**Interpretation.** Gcg and Gmg are interpreted as being the product of turbulent and cohesive debris flows, respectively. Laterally extensive beds, making up most of the exposed sequence, are interpreted as being the result of unconfined sheet floods. Most beds are capped by a clast-supported veneer inferred to represent winnowed sediments. Shallow channel bodies filled by Gmm and Gmi facies are taken to indicate, respectively, cohesive and turbulent, channelized, possibly erosive debris flow deposits. The whole section would thus be composed of gravitationally resedimented glacial sediments chiefly through the action of both channelized and unchannelized debris flows.

### 3.1.2 Site Cucao\_T1\_2

This is a road cut exhibiting a series of rounded, poorly to moderately sorted, matrix- to clast-supported gravel and sand layers disposed in  $\sim 0.1$ – $0.3$  m thick subhorizontal beds (Fig. 7e–f). Gravel is mostly within the range of pebbles. Crudely bedded, matrix-supported, chaotic and usually coarsening upwards beds (Gmm, Gmg) form laterally extensive lenses. Clast- to matrix-supported, crudely bedded and imbricated gravel layers (Gmi, Gh) alternate with parallel-stratified, pebbly sand layers (Sh) forming a series of fining

upwards sequences. Lateral extension is often truncated by concave-upwards basal surfaces of channel-shaped bodies up to 0.9–1.2 m deep filled with similar sediments. Within these fills, festoon patterns are common (St, Gt). A few outsized muddy intraclasts occur throughout the exposure.

**Interpretation.** Gmm and Gmg facies are interpreted as cohesive through turbulent debris flow deposits. Gmi, Gh and Sh are related to traction deposits under waning flow conditions associated with periodical shifts in hydraulic regime. Channel bodies' frequently truncating strata are taken as the product of a highly unstable, rapidly shifting distributary system made up of narrow, shallow channels.

### 3.1.3 Site Cucao\_T1\_3

This is a gravel pit, 8 m deep at most and topped by an organic soil unit (Fig. 7b–d). Exposure here consists of a series of poorly to moderately sorted, well-rounded, clast- to matrix-supported gravel and sand layers. Beds are between 0.1 and 0.4 m thick and several meters wide, with sharp subhorizontal or concave-upwards bounding surfaces often cutting underlying stratification at low angles. Both upward coarsening and upward fining layers occur, though the latter is more common. Beds usually show crude horizontal stratification (Gh, Sh) and trough or tabular cross-bedding (Gt–Gp, St–Sp). Small scours  $\sim 0.9$  m wide and  $\sim 0.5$  m deep filled with clast-supported, open-framework large pebbles to small cobbles (Go) are present as isolated features or within larger, 2–3 m wide and  $\sim 1.5$  m deep multistory channels. Matrix-supported, chaotic gravels (Gmm) occur almost exclusively



**Table 2.** Sediment sections analyzed in this study.

Site name	Dec. lat S/long W	Elevation (m a.s.l.)	Samples	Sediment interpretation
Cucao_T1_1	42.6585/74.0740	124	IR-50: Cucao_T1_1601	Turbulent and cohesive debris flows; unconfined sheet floods
Cucao_T1_2	42.6693/74.0905	79	IR-50: Cucao_T1_1602	Cohesive through turbulent debris flow deposits intercalated with traction deposits
Cucao_T1_3	42.6659/74.0777	112	IR-50: Cucao_T1_1603i_ii <sup>14</sup> C: Cucao_T1_1603A_A2; Cucao_T1_1803_I_II_III <sup>10</sup> Be: Cucao_T1_1601_85_115_145_175_205_235_265	Traction sediments within streamflows; deposition within a shallow braided distributary system
Cucao_T1_4	42.6681/74.0624	145	–	Main channel fill facies topped by glacial diamicton
Cucao_T1_7	42.6600/74.0752	120	<sup>14</sup> C: Cucao_T1_1804_I_II_III	Peat deposit with wood over T1 outwash
Cucao_T2_5	42.6418/74.1034	10	IR-50: Cucao_T2_1604	Braided river system within a distal ice margin environment
Cucao_T2_6	42.6418/74.0892	26	IR-50: Cucao_T2_1606; <sup>14</sup> C: Cucao_T2-1801	Braided river system within a distal ice margin environment
Till site	42.7682/73.6195	151	–	Subglacial traction till
Las Lajas site*	42.7601/73.6316	151	–	Two glacial diamictons that sandwich an 80 cm peat layer

\* García (2012).

within these fills. A few outsized, rounded, mud intraclasts lie within Sh and Gh facies.

**Interpretation.** Facies Gh, Gt–Gp, Sh and St–Sp are consistent with deposition from traction load within streamflows. Gmm facies are interpreted as debris flow deposits. Low-angle cutting is inferred to represent reactivation surfaces, reflecting a change in hydrological conditions between series of stacked traction carpets (i.e., third order surfaces in Miall, 2006). Wider multistory channel elements would represent entrenched channels active during low water stages. Altogether, deposits suggest an environment with a highly variable discharge that is prone to periodical flooding and channel instability. The whole sequence is here inferred to represent deposition within a shallow braided distributary system, with a minor contribution – or low preservation – of debris flows. The presence of mud intraclast can suggest incipient soil development within interfluvies.

### 3.1.4 Site Cucao\_T1\_4

This consists of clast-supported, poorly to moderately sorted, trough cross-bedded gravel and sand (Gt, St) (Fig. 8). They are arranged in 0.5–1 m deep and > 3 m wide channel-shaped bodies. Towards the terrace edge, an inclined erosion surface cuts through all strata and is mantled by a chaotic to crudely bedded diamicton (Dmm).

**Interpretation.** Gt–St facies in Sect. 4 are related to a channel fill. Being deeper and wider than most channels described so far, these facies could relate to the main route feeding the distributary system alluded to before. The erosion surface towards the terrace edge is interpreted as an ice-contact surface capped by melt-out till (Dmm).

### 3.1.5 Sites Cucao\_T2\_5 and \_6

Both sites occur within the edge of Cucao\_T2 terrace, near the southern coast of Lake Cucao (Fig. 3a). Exposed sedi-

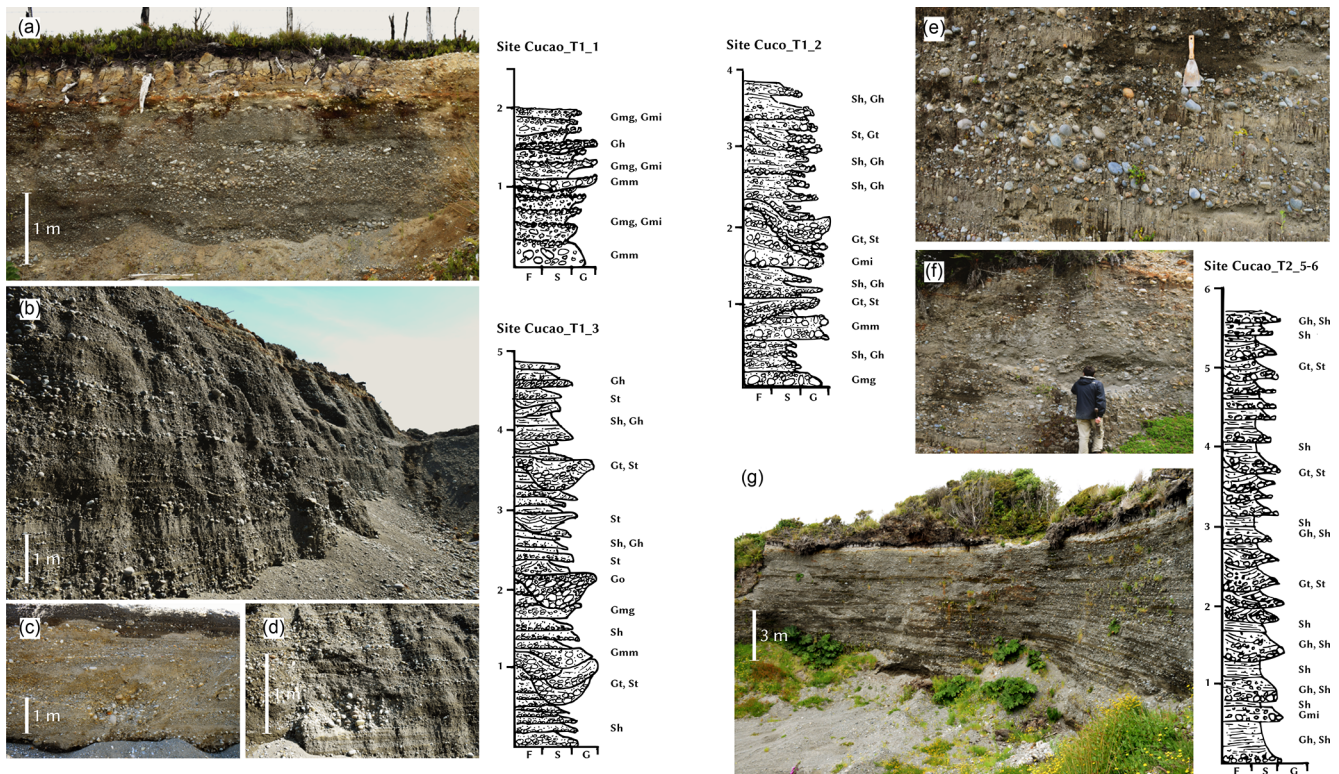


**Figure 7.** Generalized stratigraphic columns and sedimentary attributes for studied sites within Cucao terraces. (a) Cucao\_T1\_1, laterally extensive gravel beds, mostly bounded by flat subhorizontal surfaces but occasionally filling shallow channel-shaped depressions. (b) Cucao\_T1\_3 wide view. Note pebble to small cobble layer at the base of most lower bounding surfaces. (c, d) Detail of small channel bodies within Cucao\_T1\_3. Images come from two opposing walls about 3 m apart and capture the same channel element: a small open-framework gravel-filled (Go) channel in (d) grading downflow to a wider multistory filled channel in (c). This is interpreted as an entrenched gully. (e, f) Cucao\_T1\_2: (f) shows a general view capturing one of the channel-shaped bodies referred to in the description, while (e) shows a detail of stacked gravel and sand layers that characterize this exposure. (g) Cucao\_T2\_5–6, general view of sediments in Site 6. Because of similarities between both sites (5 and 6) we only show a single column that represents Cucao\_T2 sediments.



**Figure 8.** Site Cucao\_T1\_4 stratigraphic section. The image shows the two main sediment units described here. An outwash of gravel and sand (Gt, St) underlie melt-out till (Dmm); both units are separated by an ice-contact surface (white arrows), suggesting overriding ice.

ments are very similar, consisting of a series of laterally extensive, 0.1–0.5 m thick sand and pebble beds (Fig. 7g). Beds

are mostly composed of a fining-upwards sequence grading from gravel (pebbles and small cobbles) to sand. Sediment is moderately to well sorted, rounded and mostly clast-supported. Channel-shaped bodies 3–5 m wide filled with lateral accretion deposits (St-Sp; Gt-Gp) are fairly common. Beds stack on each other with flat, sharp contacts or low-angle surfaces. There are occasional channel-shaped bodies, 1–2 m thick, filled with well-rounded, well-sorted cobbles.

**Interpretation.** Dilute stream flow processes within a braided river system. This is the classical sandur deposit within a distal ice-margin environment.

### 3.1.6 The Till site

This site is located on the southern side of the Chonchi-Queilén route to the east of central Isla de Chiloé (Figs. 1 and 3b). It is a sediment pit 1.5 km to the south after the detour to Las Lajas. The pit was excavated in the southwestern side of a glacially molded hill. A hummocky terrain better characterized the surroundings including kilometer-scale hills standing several tens of meters above surround-



ing elongated depressions (Fig. 3b). The excavation walls expose several meters of indurated gravel-rich glacial diamictos making up most of the morainic relief. Sediment structures including a fissility appearance, rudimentary bedding, and well-faceted and striated clasts can be best interpreted as subglacial traction till (Fig. 9) (Menzies, 2012; Menzies et al., 2006; Evans et al., 2006). Intercalated laminated fine sediment occurs within the section, but this is not widespread.

### 3.1.7 Las Lajas site

García (2012) first described this site, located by the Las Lajas detour on the Chonchi-Queilén route (Figs. 3b and 10). It includes two glacial diamictos that sandwich an 80 cm thick peat layer. Whereas the lower diamicton–peat surface contact shows a disconformity, higher up the peat grades conformably into glaciolacustrine sediments and sands overlain by the upper diamicton. The  $^{14}\text{C}$  dates from the base and top of the peat yielded  $28.2 \pm 0.4$  and  $25.7 \pm 0.4$  cal kyr BP, respectively.

## 3.2 Chronology

### 3.2.1 Radiocarbon dating

We obtained a total of nine  $^{14}\text{C}$  samples from Cucao\_T1 and Cucao\_T2 sites (Table 3). In Site Cucao\_T1\_3 two bulk  $^{14}\text{C}$  samples from a single organic clast embedded in outwash sediment yielded  $27.7 \pm 0.2$  and  $31.5 \pm 0.3$  cal kyr BP, respectively. This clast was embedded in the sediment section nearby where we obtained the luminescence and  $^{10}\text{Be}$  samples (see below). Also in Site Cucao\_T1\_3, we obtained three  $^{14}\text{C}$  samples from wood pieces protruding out from the upper organic soil unit which ranged from  $0.2 \pm 0.07$  to  $7.5 \pm 0.07$  cal kyr BP. Site Cucao\_T1\_7 is a rather small (few tens of centimeters thick) sediment exposure on a road side where peat with wood outcrops on top of the Cucao\_T1 terrace surface. The  $^{14}\text{C}$  ages of three wood samples ranged from  $44.7 \pm 0.8$  cal kyr BP to  $> 45.0$   $^{14}\text{C}$  kyr BP.

In Cucao\_T2, we obtained an age of  $4.9 \pm 0.07$  cal kyr BP from the organic soil unit overlying the outwash sediment in Site Cucao\_T2\_6.

### 3.2.2 Luminescence dating

We obtained a total of six luminescence samples in both Cucao\_T1 (sites Cucao\_T1\_1–\_3) and Cucao\_T2 (sites Cucao\_T2\_5 and \_6). The results from high-resolution, low-level gamma spectrometry are summarized in Table 4. All samples were found to be in secular equilibrium. With regard to the equivalent dose determination, all samples showed indicators for incomplete bleaching prior to burial (right skewed dose distributions and high overdispersion values  $> 50\%$ ). Because of that, all equivalent doses were calculated using the bootstrapped MAM (Galbraith et al., 1999; Cunningham and Wallinga, 2012). The age and dose-rate cal-

culation was done using the software ADELE (Kulig, 2005). All ages were corrected for fading using the approach of Huntley and Lamothe (2001). All details are provided in Table 5.

At Site Cucao\_T1\_1 we obtained a sample (VLL-0287-L – Cucao-T1-1601) from a sand unit 100 cm below the surface and derived an age of  $33.6 \pm 3.5$  ka. At Site Cucao\_T1\_2, a single sample (VLL-0288-L – Cucao-T1-1602) was obtained from a sand lens 255 cm below the surface and yielded an age of  $51.9 \pm 6.0$  ka. At Site Cucao\_T1\_3, we obtained two samples (VLL-0289-L – Cucao-T1-1603 i and ii of which only i was dated) from the same sand unit at 350 cm below surface which yielded an age of  $56.7 \pm 5.3$  ka. From the lower Cucao\_T2 terrace, an age of  $28.1 \pm 2.6$  ka was obtained at Site Cucao\_T2\_5 (VLL-0290-L – Cucao-T2-1604) and of  $23.9 \pm 2.0$  ka at Site Cucao\_T2\_6 (VLL-0291-L – Cucao-T2-1606) at 1000 and 600 cm below surface, respectively.

### 3.2.3 The $^{10}\text{Be}$ depth profile dating

Figure 11a shows that the  $^{10}\text{Be}$  concentration declines exponentially with depth, consistent with post-deposition isotope production in a stable outwash plain and no mixing of sediment. One exception occurred towards the base of the profile where some sediment mixing could have occurred as higher concentration of  $^{10}\text{Be}$  were measured here. Our experiments show that the modeled  $^{10}\text{Be}$  age seems somewhat sensitive to the position of the original outwash surface below the top organic soil unit (20 or 35 cm) and to a lesser degree to the sediment density ( $1\sigma$  range between 1.9 and  $2.2 \text{ g cm}^{-3}$ ) (Fig. 11b iv). The modeling yielded low values for  $^{10}\text{Be}$  inheritance ( $1\sigma$  range between 0 and  $11\,000$   $^{10}\text{Be}$  atoms  $\text{g}^{-1}$ , as expected in glacial sediments; Fig. 11b iii). Based on these boundary conditions, the Cucao-T1 outwash age ranges between 45 and 100 ka (Fig. 11i, c), conditioned by the age of the organic soil formation. Accordingly, if the soil formed or was present as it is today for a short time (i.e., centennial to millennial timescales), the Cucao-T1 age would be closer to the younger limit (45 ka); alternatively, if the soil formed together with the outwash abandonment, the Cucao-T1 age would be closer to the older limit (100 ka). All other possible scenarios for organic soil formation would yield intermediate ages for Cucao-T1 outwash deposition (between 45 and 100 ka).

## 4 Discussion

### 4.1 The Cucao\_T1 and Cucao\_T2 ages

Based on the  $^{14}\text{C}$  ages obtained for the peat unit capping the outwash sediment at Site Cucao\_T1\_7, we can determine that fluvio-glacial activity linked to Cucao\_T1 ended by  $44.7 \pm 0.8$  to  $> 48.3$  cal kyr BP. In other words, the outwash minimum age is the  $^{14}\text{C}$  saturation age. This minimum age based on radiocarbon agrees with the depositional lumines-





**Figure 9.** The Till site stratigraphic section. **(a)** Geomorphic context of the section (red box) on the distal side of a drumlinoid landform (view to the south from the Las Lajas site). Ice flowed from the left (east). **(b)** Detail of the subglacial till making up most of the sediment section.

cence ages of  $51.9 \pm 6$  and  $56.7 \pm 5.3$  ka (Cucao-T1-1602 and Cucao-T1-1603 i) which occur near the younger  $^{10}\text{Be}$  model age limit. The two luminescence ages are in good agreement within error, which strengthens the reliability of the ages and the chosen luminescence dating approach. The IR-50 age obtained for Cucao-T1-1601 yielding  $33.6 \pm 3.5$  ka is not in agreement with the previous reasoning. Because all methodological steps involved to obtain that age are in agreement with the quality criteria applied for all luminescence samples in this study, the age must be regarded as a reliable luminescence age from a methodological point of view. However, there are a number of environmental uncertainties which may explain the age underestimation of that sample: this sample was taken close to the sediment surface at approximately 1 m depth. Bioturbation (plant roots, digging activities of animals) may be relevant when a sample is taken close to the surface. Although no indication of such processes was de-

tectable in the field, it cannot be ruled out that grains from the soil surface may have been relocated to deeper layers by bioturbation processes. This would result in a shift of the equivalent dose distribution to a lower dose which corresponds to a younger age. A second scenario might be that the sediment of the Cucao-T1-1601 site was locally redeposited in an event not related to the primary terrace formation. As there is no age control from radiocarbon at that site, this may have to be considered as a valid option and is further discussed in the context of the formation of the Cucao\_T2 terrace level. Considering the  $^{14}\text{C}$  ages from Site Cucao\_T1\_7, it is clear that the Cucao-T1-1601 IR-50 sample must be regarded as a minimum age for the Cucao\_T1 terrace formation.

In order to determine the age of the Cucao\_T1 terrace, we have considered two different scenarios (“a” and “b”) that best reconcile the  $^{14}\text{C}$ , IR-50 and  $^{10}\text{Be}$  chronologies obtained for this outwash. For both scenarios we have calculated the

**Table 3.** The  $^{14}\text{C}$  dates from this study.

Site name	Sample ID	Lab code	Material	$^{14}\text{C}$ age (year BP)	Error $1\sigma$ (year BP)	$2\sigma$ range calendar age (year BP)	Median probability (cal year BP)	Interpretation
Cucao_T1_3	CUCAOT1-1603A2	Beta 456717	Bulk sediment	27 820	120	31 226–31 792	31 482	Organic clast embedded in outwash sediment; likely contaminated with young carbon
Cucao_T1_3	CUCAOT1-1603A	D-AMS 020993	Bulk sediment	23 687	127	27 526–27 968	27 747	Organic clast embedded in outwash sediment; likely contaminated with young carbon
Cucao_T1_3	CUCAOT1-1803_I	D-AMS 031033	Wood	772	25	649–722	672	Minimum age of soil on top of Cucao_T1 outwash
Cucao_T1_3	CUCAOT1-1803_II	D-AMS 031034	Wood	6591	40	7415–7565	7461	Minimum age of soil on top of Cucao_T1 outwash
Cucao_T1_3	CUCAOT1-1803_III	D-AMS 031035	Wood	188	25	135–283	182	Minimum age of soil on top of Cucao_T1 outwash
Cucao_T1_7	CUCAOT1-1804_I	D-AMS 031036	Wood	> 45 000		> 47 030–49 603	> 48 312	Minimum age for Cucao_T1 outwash deposition/abandonment
Cucao_T1_7	CUCAOT1-1804_II	D-AMS 031037	Wood	41 781	496	44 245–46 012	45 127	Minimum age for Cucao_T1 outwash deposition/abandonment
Cucao_T1_7	CUCAOT1-1804_III	D-AMS 031038	Wood	41 273	411	43 905–45 481	44 713	Minimum age for Cucao_T1 outwash deposition/abandonment
Cucao_T2_6	CUCAOT2-1801	D-AMS 031053	Bulk sediment	4391	31	4843–4979	4919	Minimum age of soil on top of Cucao_T2 outwash

**Table 4.** Results from radionuclide analysis and dose-rate calculation.

Sample lab code	Sample field code	$^{238}\text{U}$ ( $\text{Bq kg}^{-1}$ )	$^{232}\text{Th}$ ( $\text{Bq kg}^{-1}$ )	$^{40}\text{K}$ ( $\text{Bq kg}^{-1}$ )	Overall dose-rate Fs ( $\text{Gy kyr}^{-1}$ ) <sup>a</sup>
VLL-0287-G	Cucao_T1 1601	$14.7 \pm 1.1$	$21.5 \pm 1.8$	$314.0 \pm 18.9$	$2.41 \pm 0.17$
VLL-0288-G	Cucao_T1 1602	$14.8 \pm 1.2$	$21.8 \pm 1.2$	$342.0 \pm 20.5$	$2.45 \pm 0.17$
VLL-0289-G	Cucao_T1 1603i/ii <sup>b</sup>	$15.7 \pm 1.1$	$21.5 \pm 1.2$	$351.0 \pm 21.1$	$2.47 \pm 0.18$
VLL-0290-G	Cucao_T2 1604	$15.1 \pm 1.2$	$20.3 \pm 1.1$	$341.0 \pm 20.5$	$2.49 \pm 0.17$
VLL-0291-G	Cucao_T2 1606	$13.9 \pm 1.0$	$20.0 \pm 1.3$	$333.0 \pm 20.0$	$2.33 \pm 0.16$

<sup>a</sup> Cosmic dose rate determined according to Prescott and Stephan (1982) and Prescott and Hutton (1994), taking the geographical position of the sampling spot (longitude, latitude, and altitude), the depth below surface and the average density of the sediment overburden into account. An uncertainty of 10 % was assigned to the calculated cosmic dose rate. External and internal dose rate calculated using the conversion factors of Adamiec and Aitken (1998) and the  $\beta$ -attenuation factors of Mejdahl (1979), including an  $\alpha$ -attenuation factor of  $0.08 \pm 0.01$ , an internal K content of  $12.5 \pm 0.5$  % (Huntley and Baril, 1997) and an estimated average water content of  $15 \pm 5$  % throughout burial time. Values covering almost dry to almost saturated conditions. Error was propagated to the overall dose-rate calculation. <sup>b</sup> Only sample Cucao\_T1 1603i was measured because both samples were taken in direct vicinity from the same sediment layer.

probability distributions in Bayesian terms. In both scenarios, all ages obtained for the Cucao\_T1 outwash deposition are older than the  $^{14}\text{C}$  ages from Site Cucao\_T1\_7. The scenario “a” considers the  $^{10}\text{Be}$  age as a minimum (i.e., corresponding to a short-lived organic soil development) and

the luminescence ages as the depositional age of the outwash sediment. The scenario “b” considers the wide  $^{10}\text{Be}$  age range (i.e., corresponding to an organic soil development at any time since the Cucao\_T1 outwash abandonment), together with the luminescence ages, as the deposi-

**Table 5.** Summary of IR-50 data.

Sample lab code	Sample field code	Fs SG (n) <sup>1</sup>	$\sigma b^2$ (%)	Fs IR-50 D <sub>e</sub> (Gy) <sup>3</sup>	Dose rate Fs (Gy kyr <sup>-1</sup> ) <sup>4</sup>	Fs IR-50 age (ka) faded <sup>5</sup>	Fs IR-50 age (ka) fading corr. <sup>6</sup>
VLL-0287-L	Cucao_T1 1601	83	67 ± 6	50.5 ± 3.5	2.41 ± 0.17	20.9 ± 2.1	33.6 ± 3.5
VLL-0288-L	Cucao_T1 1602	78	51 ± 5	78.3 ± 4.9	2.45 ± 0.17	31.9 ± 3.0	51.9 ± 6.0
VLL-0289-L	Cucao_T1 1603i/ii	83	50 ± 4	85.9 ± 3.8	2.47 ± 0.18	34.8 ± 2.9	56.7 ± 5.3
VLL-0290-L	Cucao_T2 1604	82	73 ± 6	43.9 ± 2.5	2.49 ± 0.17	17.6 ± 1.5	28.1 ± 2.6
VLL-0291-L	Cucao_T2 1606	197	71 ± 4	34.9 ± 1.7	2.33 ± 0.16	15.0 ± 1.3	23.9 ± 2.0

<sup>1</sup> Number of single grains (SGs) passing all rejection criteria. <sup>2</sup> Overdispersion calculated using the CAM (Galbraith et al., 1999). <sup>3</sup> Equivalent dose (D<sub>e</sub>) calculated using the bootstrapped MAM-3 (Galbraith et al., 1999; Cunningham and Wallinga, 2012) for all samples. <sup>4</sup> Overall dose rate. <sup>5</sup> Ages calculated using the software ADELE (Kulig, 2005). <sup>6</sup> Fs-based ages corrected for fading according to the method of Huntley and Lamothe (2001) using the R luminescence package (Kreutzer et al., 2012).

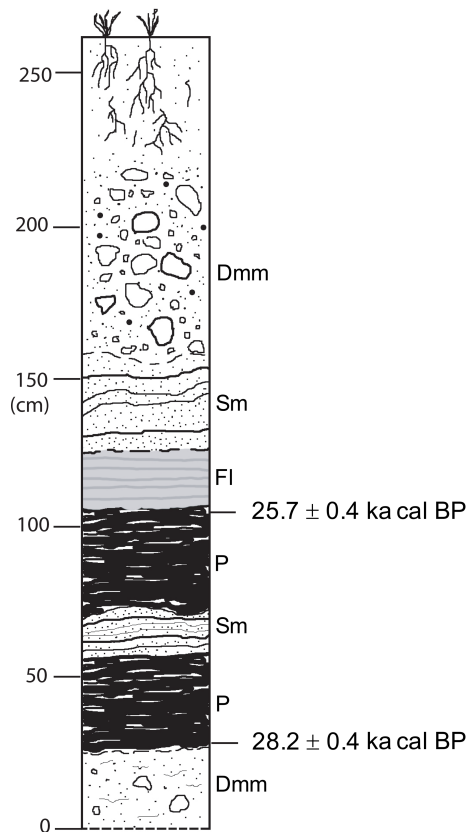


**Figure 10.** Stratigraphic column of the Las Lajas site. Two diamictons (Dmm) sandwich a peat soil (P) and inorganic glacial finer sediments (Sm, Fl). The upper peat layer dates a glacial advance on the site as evidenced by the upward coarsening of the sediments. Modified from García (2012).

tional ages of the outwash. For scenario “a”, the resulting age is  $57.8 \pm 4.7$  ka, and for scenario “b” the resulting age is  $55.5^{+29}_{-6.5}$  ka.

The data show that both scenarios yield statistically the same most likely age but differ in precision (Figs. 12a, b). The overlap between luminescence ages and <sup>10</sup>Be fitting models (youngest outwash ages in Fig. 11c) suggest that

most of the organic soil unit has been in its present form and thickness for a limited time span. The older <sup>14</sup>C ages (Site 7) also suggest that scenario “a” is most probable, which implies that the shielding of cosmogenic radiation by the organic unit has not been significant since the Cucao\_T1 outwash deposition (MIS 3). A question may arise regarding the range of <sup>14</sup>C ages we obtained from the organic sediment capping the Cucao\_T1 outwash in two different sites, including MIS 3 (Cucao\_T1\_Site 7) and Holocene (Site 3) dates. Taking the data at face value, and in the light of <sup>10</sup>Be and IR-50 data, it is unlikely that an organic soil as thick (and dense) as in Site Cucao\_T1\_7 has been present since  $\geq 48.3 \pm 1.3$  cal kyr BP. The implication is that the top organic soil was not preserved throughout the MIS 3 and MIS 2 until the present. In fact, we do not find MIS 3 but only Holocene <sup>14</sup>C ages in Site 3, supporting a young organic cover (Table 3). This points to an unsteady organic layer cover (e.g., mostly absent or of limited thickness) after the Cucao\_T1 deposition. Therefore, our preferred modeled age, when IR-50, <sup>10</sup>Be and <sup>14</sup>C data match, is  $57.8 \pm 4.7$  ka for the Cucao\_T1 outwash deposition. This age identifies the early Llanquihue Glaciation in Chiloé (i.e., the ILGM).

The two luminescence IR-50 ages obtained from samples related to the Cucao\_T2 terrace yielded ages in good agreement within error. The calculated mean age of  $26.0 \pm 2.9$  ka obtained for the Cucao\_T2 terrace corroborates that this terrace represents a younger, inboard glacial extent. The increased geomorphic activity in the area during the formation of the Cucao\_T2 terrace level likely included enhanced incision into the Cucao\_T1 terrace level and increased remobilization of sediments on the Cucao\_T1 terrace. This initial phase of climate deterioration potentially resulted in the remobilization of material on the Cucao\_T1 terrace level, followed by incision and subsequent build-up of the Cucao\_T2 terrace on a lower level. The initial phase of remobilization and incision may be represented by the IR-50 age of sample Cucao-T1-1601, which was taken close to the present Cucao\_T1 terrace surface (and present-day Cucao\_T1–Cucao\_T2 scarp) and yielded an age of  $33.6 \pm$



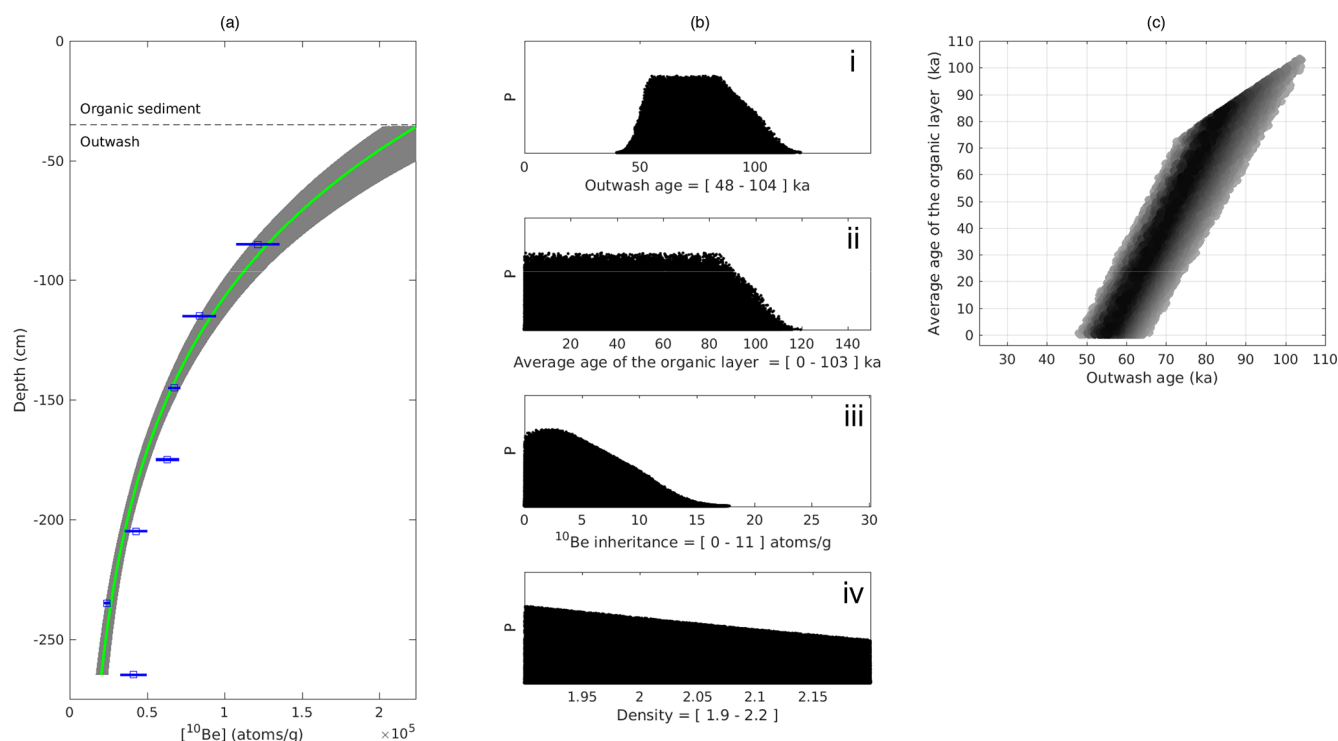


**Figure 11.** Site Cucao\_T1\_3  $^{10}\text{Be}$  depth profile results. (a) Depth profile with cosmogenic samples and vertical distribution of the outwash and the overlaying organic sediments: Be-10 data in blue, best fit of the Be-10 accumulation models in green and  $1\sigma$  fitting models in grey. (b) Probability density distributions of the parameters considered in the models shown in (a). (c) The  $1\sigma$  results of the fitting ages for the deposition of the outwash and the organic layer in different shades of grey based on their probabilities.

3.5 ka, which is only slightly older than the luminescence ages obtained from the Cucao\_T2 terrace sediments.

#### 4.2 The local LGM ice limit

Based on the mapping, sediment preservation and age of the landforms, each Cucao outwash plain Cucao\_T1 and Cucao\_T2 could be linked to expanded ice marginal positions within the last glacial period (Fig. 3a). García (2012) mapped a double Llanquihue age ice-contact slope widespread on the eastern slope of the Cordillera de la Costa that was linked to a double system of outwash terraces on the western mountainside, such as Cucao\_T1 and Cucao\_T2. In this scenario, the PIS buttressed against the Cordillera de la Costa (here up to  $\sim 500$  m a.s.l.), which acted as a barrier for the Golfo de Corcovado Ice Lobe's expansion towards the open Pacific Ocean. The mountain range is punctuated by meltwater channels that grade to the outwash plains to the west. Opposite, the Huillenco–Cucao basin (Fig. 1) allowed a narrow tongue of ice to flow through the coastal mountains. Here, the exact ice marginal positions attained during the Cucao\_T1 and Cucao\_T2 outwash depositions are not obvious. It is possible that part of the scarp separating Cucao\_T1 from Cucao\_T2 can be regarded as a reworked ice contact slope (Fig. 3a). Several sources of evidence could support this scenario indicating ice proximity: (1) a glacial diamicton outcropping

at the proximal edge of T1 in Site Cucao\_T1\_4, (2) the Cucao\_T1 terrace high dipping angle of  $\sim 2\%$  and (3) the ice proximal facies (e.g., debris flows) intercalated with better sorted outwash outcroppings in the studied sediment sections within Cucao\_T1 terrace (Figs. 7 and 8). On the other hand, the lower Cucao\_T2 deposition can be linked to an in-board ice margin at the proximal edge of this outwash plain (Fig. 3a). The morainic relief confining the Quilque lake can be interpreted as a hummocky moraine formed as part of a dead-ice topography related to the deglacial phase after the terminal position against the ice contact slope of Cucao\_T1 terrace or, alternatively, as a push complex during active ice recession (Evans and Twigg, 2002). Sediment slumps from the T1 ice-contact slope during a paraglacial phase are also a possibility during deglaciation.

The inferred ice limits imply that ice reached more or less similar positions, first at  $57.8 \pm 4.7$  ka (Cucao\_T1 terrace) and then  $26.0 \pm 2.9$  ka (Cucao\_T2 terrace), with ice covering most of the island to the Cordillera de la Costa or slightly beyond this point along the Huillenco–Cucao basin.

An extended ice position to the Cordillera de la Costa at  $26.0 \pm 2.9$  ka may be in conflict with a previous interpretation of the Las Lajas site (García, 2012). Here, the upper diamicton was interpreted as being deposited at the ice margin by  $25.7 \pm 0.4$  cal kyr BP. This ice advance was pre-

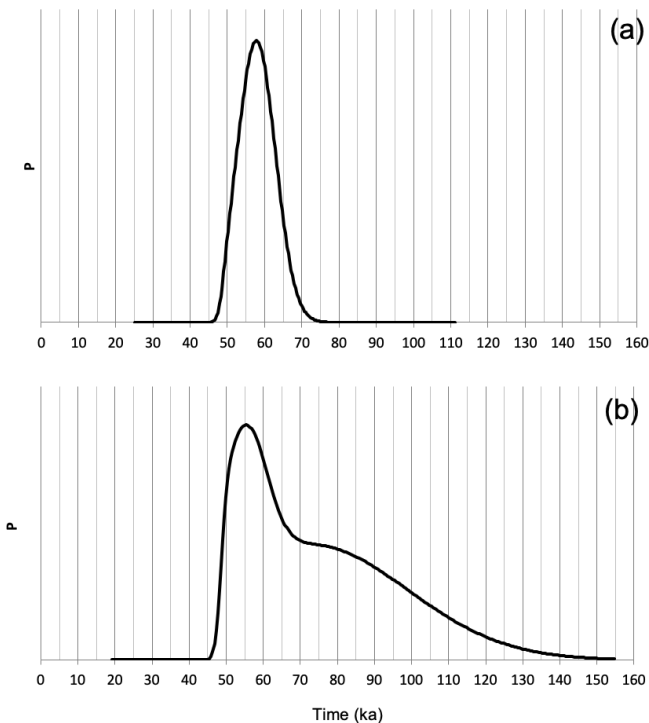


**Figure 12.** Scenarios “a” and “b” probability distributions of  $^{10}\text{Be}$ ,  $^{14}\text{C}$  and IR-50 data. Both scenarios coincide in the best Bayesian age but differ in terms of precision. In (a), scenario “a” considers that the organic soil as it is today has been present in the site for only a short time (centuries to millennia). The kernel density estimation of the age of the outwash has been calculated as  $p(\text{TOSL}|t) \cdot p(T^{14}\text{C} < t) \cdot p(T^{10}\text{Be} < t)$ , where  $p(\text{TOSL}|t)$  is the sum of the probabilities corresponding to the IR-50 ages, and  $p(t > T^{14}\text{C})$  and  $p(t > T^{10}\text{Be})$  are the cumulative sum of the probabilities corresponding to the minimum  $^{14}\text{C}$  and  $^{10}\text{Be}$  ages, respectively. In this case, we only considered the probabilities of the minimum  $^{10}\text{Be}$  age corresponding to an age of 0 for the organic soil ( $y = 0$  in Fig. 11c;  $56.5 \pm 8.5$   $^{10}\text{Be}$  ka). In (b), scenario “b” considers that the organic soil was formed anytime between outwash deposition and today. The kernel density estimation of the age of the outwash has been calculated as  $p(\text{TOSL}|t) \cdot p(T^{14}\text{C} < t) \cdot p(T^{10}\text{Be}|t)$ , where  $p(T^{10}\text{Be}|t)$  corresponds to the  $^{10}\text{Be}$  age obtained in Fig. 11 (72.5  $\pm$  26.5  $^{10}\text{Be}$  ka). Note that here only the  $^{14}\text{C}$  ages are considered as minimum ages.

ceded by ice-free conditions interpreted from the peat layer between  $28.2 \pm 0.4$  and  $25.7 \pm 0.4$  cal kyr BP when ice should have resided up-glacier from the Las Lajas site (i.e., reduced ice standing to the east of Isla de Chiloé). Then, the Cucao\_T2 outwash deposition can only have occurred between 26 cal kyr BP and 23.1 ka, if the age control from both sites (the IR-50 and  $^{14}\text{C}$  ages) is considered using  $1\sigma$  range. Several lines of evidence suggest that the ice expanded westward to the Cordillera de la Costa by  $25.7 \pm 0.4$  cal kyr BP to deposit the Cucao\_T2 terrace. First, it seems difficult to reconcile an ice margin at eastern Chiloé building the western Cucao\_T2 outwash plain  $\geq 20$  km away. No topographic

match seems plausible. Second, ice must have overridden Las Lajas when it expanded westward to the Cordillera de la Costa. Third, nearby sediment and the geomorphic record denote that subglacial morphogenesis originated by overriding ice. The Till site, near Las Lajas, exposes well-preserved subglacial traction till (Figs. 3b and 9). Nearby exposures along the Chonchi-Queilén route in eastern Chiloé (Fig. 1) commonly denote outwash sediments being capped with erosional surfaces by glacial diamictons, showing overriding ice during ice expansion (García, 2012). Fluting and drumlinoid landforms cored by till then can suggest that rapid-flowing ice expanded all the way to the Cordillera de la Costa in central Chiloé during the Llanquihue Glaciation. In the light of the new morphostratigraphic observations and geochronologic data, we thus suggest the Golfo de Corcovado Ice Lobe expanded towards the Cordillera de la Costa to deposit the Cucao\_T2 outwash by  $25.7 \pm 0.4$  cal kyr BP, thus overriding central Chiloé during the global LGM. Just north in the CLD, glaciers reached their most extensive positions by about 26 ka also, as suggested by Denton et al. (1999b). Antarctic ice cores show stadial conditions between  $\sim 28$  and 24 ka peaking at  $\sim 26$  ka that seem to be mirrored by SST off-shore Chiloé (WAIS Divide Project Members, 2015; Lamy et al., 2004).

#### 4.3 The pre-LGM Llanquihue Glaciation

Precise geochronologic records of glacial activity during the early to middle MIS 3 are rare in the CLD. Moreover, no records of MIS 4 glaciation exist on land. On the other hand, available radiocarbon data have precisely constrained glacial fluctuations during the LGM (Mercer, 1972, 1976; Porter, 1981; Denton et al., 1999b). Therefore, only a limited understanding of glacial fluctuations during pre-LGM time exists today. Available dating for the early Llanquihue drift is mostly equivocal because either the stratigraphic context is not well understood or dates reported are not sufficiently precise ages for dating putative pre-LGM glacial advance(s) (Porter, 1981; Denton et al., 1999b). For instance, the “crossroad stratigraphic site” west of Lago Llanquihue (Denton et al., 1999b; Porter, 1981; Mercer, 1976) includes deformed weathered pyroclastic organic sediments including wood and charcoal sandwiched by pre-Llanquihue (below) and Llanquihue (above) till. Minimum ages ranging from  $> 39.6 \pm 0.7$  to  $57.8$   $^{14}\text{C}$  kyr BP obtained from the non-glacial sediments do not closely constrain the age of glacial advances represented by the till units. Nearby the “crossroad site”, a reworked organic clast into Llanquihue outwash yielded  $> 44.4$   $^{14}\text{C}$  kyr BP (Denton et al., 1999b; Mercer, 1976). Similarly, the bottom sediments of the Puerto Octay and the Bahía Frutillar Bajo sections show Llanquihue drifts deposited before  $41.3 \pm 0.7$  and  $45.4 \pm 2.0$  cal kyr BP, respectively (Denton et al., 1999b). To the north, an early Llanquihue glacial advance  $> 56.0$   $^{14}\text{C}$  kyr BP occurred in Lago Ranco, as suggested by  $^{14}\text{C}$  dating of a log in peat

that occurs stratigraphically linked to interpreted till sediments (Mercer, 1976). Porter (1981) reported a wood age of  $45.7 \pm 1.0$  cal kyr BP from an interdrift in situ stump in Punta Penas. In Punta Pelluco, wood in a similar stratigraphic context yielded  $> 40.0$   $^{14}\text{C}$  kyr BP (Porter, 1981). All these records suggest Llanquihue glacial expansions during pre-LGM times, but it remains unclear the precise dates of the events. In contrast, the Taikemó record in Chiloé provides unique details regarding the Llanquihue Glaciation (Heusser et al., 1999). The Taikemó mire is located inboard from the outermost early Llanquihue moraine. The basal minimum limiting age of Taikemó of  $> 49.9$   $^{14}\text{C}$  kyr BP suggests this early Llanquihue landform was deposited by this time. Dating of the Taikemó basal sediments beyond the  $^{14}\text{C}$  technique suggest that an early glacial maximum occurred before  $> 50.0$   $^{14}\text{C}$  kyr BP when a pollen peak in Gramineae overlaps with a jump in magnetic susceptibility and a minimum in loss on ignition (Heusser et al., 1999).

Although dating control is limited (i.e., available dates occur at the limit and beyond the  $^{14}\text{C}$  possibilities,  $> 50$   $^{14}\text{C}$  kyr BP), evidence suggests that interstadial periods dominated by tree species adapted to cool and humid conditions occurred during the MIS 3 (Heusser et al., 1999; Villagrán et al., 2004, 2019). A reasonable scenario is that these ecosystems spread during the Antarctic millennial-scale interstadial periods that punctuated the MIS 3, for instance, at  $\sim 60$  ka (Antarctic Isotope Maximum, AIM, 17) and/or at  $\sim 54$  ka (AIM 14) (WAIS Divide Project Members, 2015). Near the base of the Taikemó record a peak in warm temperatures was interpreted from a broad peak in loss of ignition and a Gramineae minimum within subantarctic evergreen forest conditions (Heusser et al., 1999) which could have been accompanied by the expansion of conifer forest to the low lands of Chiloé (Villagrán et al., 2004). Therefore, we suggest that the Cucao\_T1 glacial advance was triggered by a millennial-scale climate deterioration that followed an interstadial peak (e.g., the AIM 17). This PIS glacial expansion by  $57.8 \pm 4.7$  ka into the outermost ice-contact slope in Chiloé coincided with a decreasing SST trend that lasted several millennia and culminated offshore Chiloé  $\sim 4\text{--}5^\circ\text{C}$  below the early Holocene value (Kaiser et al., 2005). The Antarctic temperature stack (Parrenin et al., 2013), which mimics the WAIS divide ice core  $\delta^{18}\text{O}$  record (WAIS Divide Project Members, 2015), records a stadial period culminating at  $\sim 57$  ka when atmospheric temperatures reached  $6\text{--}7^\circ\text{C}$  below those of the present day. Presumably, during this Antarctic stadial the westerly wind belt shifted north, associated with extended sea ice and the expansion of Antarctic and subantarctic atmospheric and oceanic conditions into lower latitudes (Lamy et al., 2015). The expanded westerly wind belt linked to an enhanced northern ACC boundary brought depressed SST and air temperatures and high precipitation to the latitude of Chiloé, thus forcing a PIS advance here by the early MIS 3.

#### 4.4 MIS 3 paleoclimate

This section discusses the MIS 3 paleoclimate in the context of glacial fluctuations of the PIS and other Southern Hemisphere mountain glaciers. Globally, the MIS 3 is a long-term interstadial phase when ice sheets were reduced, sea level reached intermediate stands, and temperatures were mild (Shackleton et al., 2000; Ivy-Ochs et al., 2008; Parnucci et al., 2012; Dalton et al., 2019). The peak of the MIS 3 warmth occurred at  $\sim 60$  ka, the first in a sequence of prominent millennial-scale climate changes (e.g., Dansgaard-Oeschger and AIM events) recorded at both polar hemispheres during this period (Jouzel et al., 2007). Nonetheless, the climate variability in the MIS 3 is conspicuous not only in the polar records but elsewhere (Mayr et al., 2019).

After MIS 4, climate in New Zealand and southern Chile was rather mild. In New Zealand, the Aurora Interstadial lasted until about 43 ka, but it was interrupted by stadial conditions, first at 49–47 ka and then at 42–38 ka, when Southern Alps glaciers readvanced (Williams et al., 2015; Kelley et al., 2014; Doughty et al., 2015). Between 37–31 ka, a new phase of mild interstadial temperatures was recorded in New Zealand, after which temperatures declined into the MIS 2 global LGM phase (Putnam et al., 2013; William et al., 2015; Darvill et al., 2016). In southern Chile, Heusser et al. (1999) recorded interstadial temperatures and humid conditions until about  $> 50$  ka when temperatures started a cooling trend that extended until the global LGM. Ice-free areas later overridden by glacier or ice proximal outwash deposits occurred between about 43–33 ka, thus indicating mid-to-late MIS 3 ice fluctuations (Denton et al., 1999b). Similarly, high and low frequencies of Gramineae punctuated the MIS 3, thus being indicative of millennial-scale temperature changes throughout the MIS 3 (Heusser et al., 1999). Distal to the PIS front, interstadial conifer forests are known to have grown in areas later overridden by ice, as recorded by peat layers containing tree trunks on sea-cliff exposures and also by tree stumps standing in life position at present-day intertidal sea shores (Roig et al., 2001; Villagrán et al., 2004, 2019). Along the eastern coastal cliffs of Chiloé multiple peat layers are intercalated with finely laminated glacial sediments assumed to be early MIS 3 in age, suggesting short-term environmental variability (Villagrán et al., 2004, 2019). Moreover, these glacial-sourced sediments suggest that the PIS front, although located up ice from Isla de Chiloé, was not much further to the east during the MIS 3. A similar conclusion can be derived from the alternating peat and lake facies that punctuate the Taikemó record between about  $> 50\text{--}40$  ka (Heusser et al., 1999). Altogether, the available records show that not only did mild atmospheric conditions punctuate the MIS 3, but rather this was a variable climatic period both in the middle and high latitudes. In fact, Lovejoy and Lambert (2019) noted that the highest climate variability occurs during the middle of a glacial cycle (e.g., MIS 3), the opposite being true at the ends (i.e., the LGM) when a rather stable climate pre-



dominates. These authors studied the European Project for Ice Coring in Antarctica (EPICA) dust flux frequency record, which is known to be linked to Patagonian climate and glacial fluctuations, among others factors (Lambert et al., 2008), and which therefore provides a direct link between southern middle and high latitudes (Sugden et al., 2009; Kaiser and Lamy, 2010). During mid-glacial climates, transition times and amplitudes of Antarctic dust flux variability occurred at centennial to millennial timescales implying that large PIS ice lobe extent variability occurred also at these time frequencies in response to climate change forcing (see Lovejoy and Lambert, 2019). Therefore, an extensive northern PIS glacial expansion at  $57.8 \pm 4.7$  ka in Chiloé, together with that recorded by the PIS in Torres del Paine, Última Esperanza and Bahía Inútil by  $\sim 48$  ka (Sagredo et al., 2011; Darvill et al., 2015; García et al., 2018) and in New Zealand at  $\sim 49$ – $47$  and  $42$ – $38$  ka (Kelley et al., 2014; William et al., 2015), suggests a distinct return to glacial conditions in the southern midlatitudes within the MIS 3.

## 5 Conclusions

Full glacial advances by the Golfo de Corcovado Ice Lobe of the northwest Patagonian Ice Sheet (PIS) occurred by  $57.8 \pm 4.7$  and  $26.0 \pm 2.9$  ka on the Isla de Chiloé and respectively deposited the outer Cucao\_T1 and Cucao\_T2 outwash plains enclosing the Lago Cucao basin. The latter ice advance could be tied to a previously dated advance to  $25.7 \pm 0.3$  cal kyr BP that better constrains its age (García, 2012). The extent of the now inexistent Golfo de Corcovado Ice Lobe was  $> 100$  km during both glacial expansions, which did not reach the Pacific Ocean during the Llanquihue Glaciation. The early Llanquihue ice expansion during the MIS 3 occurred intercalated with interstadial periods, which denotes the sensitive response of the Patagonian glaciers to centennial- to millennial-scale climate fluctuations. Southern midlatitude glacial advances interrupting the apparent mild climate that characterized the early MIS 3 imply that this time period was rather characterized by large and rapid climate oscillations not only at the poles but elsewhere.

**Code availability.** All details with regard to the codes used in this study are available from the references provided in the text. The primary sources also contain information about the availability of the code.

**Data availability.** All relevant data have been included in the published version of this paper. Otherwise, please submit any requests to jgarciab@uc.cl.

**Author contributions.** JLG conceived the project. JLG and RMV collected the  $^{10}\text{Be}$ , IR-50 and  $^{14}\text{C}$  samples and performed the sed-

iment description in the field. ASH and SAB performed the  $^{10}\text{Be}$  laboratory and AMS work. JLG performed the  $^{14}\text{C}$  laboratory work. CL performed the IR-50 laboratory work and luminescence age calculation. AR and ASH performed the  $^{10}\text{Be}$  and Bayesian modeling. All authors contributed to interpret the data and write the paper.

**Competing interests.** The authors declare that they have no conflict of interest.

**Acknowledgements.** The authors acknowledge the support from the Chile FONDECYT. We thank the valuable comments of two reviewers that improved the quality of this paper.

**Financial support.** This research has been supported by the Chile FONDECYT (grant no. 1161110).

The article processing charge was funded by the Quaternary scientific community, as represented by the host institution of EGQSJ, the German Quaternary Association (DEUQUA).

**Review statement.** This paper was edited by Becky Briant and reviewed by Gordon Bromley and one anonymous referee.

## References

- Adamiec, G. and Aitken, M.: Dose-rate conversion factors: update, *Ancient TL*, 16, 37–50, 1998.
- Andersen, B. G., Denton, G. H., and Lowell, T. V.: Glacial geomorphologic maps of Llanquihue drift in the area of the southern Lake District, Chile, *Geogr. Ann. A*, 81, 155–166, <https://doi.org/10.1111/1468-0459.00056>, 1999.
- Auclair, M., Lamothe, M., and Huot, S.: Measurement of anomalous fading for feldspar IRSL using SAR, *Radiat. Meas.*, 37, 487–492, [https://doi.org/10.1016/S1350-4487\(03\)00018-0](https://doi.org/10.1016/S1350-4487(03)00018-0), 2003.
- Balco, G., Stone, J. O., Lifton, N. A., and Dunai, T. J.: A complete and easily accessible means of calculating surface exposure ages or erosion rates from  $^{10}\text{Be}$  and  $^{26}\text{Al}$  measurements, *Quat. Geochronol.*, 3, 174–195, <https://doi.org/10.1016/j.quageo.2007.12.001>, 2008.
- Barcaza, G., Nussbaumer, S. U., Tapia, G., Valdés, J., García, J. L., Videla, Y., Albornoz, A., and Arias, V.: Glacier inventory and recent glacier variations in the Andes of Chile, South America, *Ann. Glaciol.*, 58, 166–180, <https://doi.org/10.1017/aog.2017.28>, 2017.
- Bentley, M. J.: Relative and radiocarbon chronology of two former glaciers in the Chilean Lake District, *J. Quaternary Sci.*, 12, 25–33, [https://doi.org/10.1002/\(SICI\)1099-1417\(199701/02\)12:1<25::AID-JQS289>3.0.CO;2-A](https://doi.org/10.1002/(SICI)1099-1417(199701/02)12:1<25::AID-JQS289>3.0.CO;2-A), 1997.
- Bierman, P. R., Caffee, M. W., Davies, P. D., Marsella, K., Pavich, M., Colgan, P., Mickelson, D., and Larsen, J.: Rates and Timing of Earth Surface Processes From In Situ-Produced Cosmogenic Be-10, *Rev. Mineral. Geochem.*, 50, 147–205, <https://doi.org/10.2138/rmg.2002.50.4>, 2002.

- Blomdin, R., Murray, A., Thomsen, K., Buylaert, J.-P., Sohbati, R., Jansson, K., and Alexanderson, H.: Timing of the deglaciation in southern Patagonia: Testing the applicability of K-Feldspar IRSL, *Quat. Geochronol.*, 10, 264–272, <https://doi.org/10.1016/j.quageo.2012.02.019>, 2012.
- Bøtter-Jensen, L., Bulur, E., Duller, G., and Murray, A.: Advances in luminescence instrument systems, *Radiat. Meas.*, 32, 523–528, [https://doi.org/10.1016/S1350-4487\(00\)00039-1](https://doi.org/10.1016/S1350-4487(00)00039-1), 2000.
- Bøtter-Jensen, L., Andersen, C., Duller, G., and Murray, A.: Developments in radiation, stimulation and observation facilities in luminescence measurements, *Radiat. Meas.*, 37, 535–541, [https://doi.org/10.1016/S1350-4487\(03\)00020-9](https://doi.org/10.1016/S1350-4487(03)00020-9), 2003.
- Cunningham, A. and Wallinga, J.: Realizing the potential of fluvial archives using robust OSL chronologies, *Quat. Geochronol.*, 12, 98–106, <https://doi.org/10.1016/j.quageo.2012.05.007>, 2012.
- Dalton, A. S., Finkelstein, S. A., Forman, S. L., Barnett, P. J., Pico, T., and Mitrovica, J. X.: Was the Laurentide Ice Sheet significantly reduced during Marine Isotope Stage 3? *Geology*, 47, 111–114, <https://doi.org/10.1130/G45335.1>, 2019.
- Darvill, C. M., Bentley, M. J., Stokes, C. R., Hein, A. S., and Rodés, A.: Extensive MIS 3 glaciation in southernmost Patagonia revealed by cosmogenic nuclide dating of outwash sediments, *Earth Planet. Sc. Lett.*, 429, 157–169, <https://doi.org/10.1016/j.epsl.2015.07.030>, 2015.
- Darvill, C. M., Bentley, M. J., Stokes, C. R., and Shulmeister, J.: The timing and cause of glacial advances in the southern mid-latitudes during the last glacial cycle based on a synthesis of exposure ages from Patagonia and New Zealand, *Quaternary Sci. Rev.*, 149, 200–214, <https://doi.org/10.1016/j.quascirev.2016.07.024>, 2016.
- Davies, B. J., Darvill, C. M., Lovell, H., Bendle, J. M., Dowdeswell, J. A., Fabel, D., García, J.-L., Geiger, A., Glasser, N. F., Gheorghiu, D. M., Harrison, S., Hein, A. S., Kaplan, M. R., Martin, J. R. V., Mendelova, M., Palmer, A., Pelto, M., Rodés, A., Sagredo, E. A., Smedley, R., Smellie, J. L., and Thorndyck, V. R.: The evolution of the Patagonian Ice Sheet from 35 ka to the present day (PATICE), *Earth-Sci. Rev.*, 204, 103152, <https://doi.org/10.1016/j.earscirev.2020.103152>, 2020.
- Denton, G. H., Heusser, C. J., Lowell, T. V., Moreno, P. I., Andersen, B. G., Heusser, L. E., Schlüchter, C., and Marchant, D. R.: Interhemispheric linkage of paleoclimate during the last glaciation, *Geogr. Ann. A*, 81, 107–153, <https://doi.org/10.1111/1468-0459.00055>, 1999a.
- Denton, G. H., Lowell, T. V., Moreno, P. I., Andersen, B. G., and Schlüchter, C.: Geomorphology, stratigraphy, and radiocarbon chronology of Llanquihue Drift in the area of the Southern Lake District, Seno de Reloncaví and Isla Grande de Chiloé, *Geogr. Ann. A*, 81, 167–229, <https://doi.org/10.1111/1468-0459.00057>, 1999b.
- Dewald, A., Heinze, S., Jolie, J., Zilges, A., Dunai, T., Rethemeyer, J., Melles, M., Staubwasser, M., Kuczewski, B., Richter, J., Radtke, U., von Blanckenburg, F., and Klein, M.: CologneAMS, a dedicated center for accelerator mass spectrometry in Germany, *Nucl. Instrum. Meth. B*, 294, 18–23, <https://doi.org/10.1016/j.nimb.2012.04.030>, 2013.
- Doughty, A. M., Schaefer, J. M., Putnam, A. E., Denton, G. H., Kaplan, M. R., Barrell, D. J. A., Andersen, B. G., Kelley, S. E., Finkel, R. C., and Schwartz, R.: Mismatch of glacier extent and summer insolation in Southern Hemisphere mid-latitudes, *Geology*, 43, 407–410, <https://doi.org/10.1130/G36477.1>, 2015.
- Duller, G. A. T.: Single grain optical dating of glacial deposits, *Quat. Geochronol.*, 1, 296–304, <https://doi.org/10.1016/j.quageo.2006.05.018>, 2006.
- Evans, D. J. A. and Twigg, D. R.: The active temperate glacial landsystem: a model based on Breiðamerkurjökull and Fjallsjökull, Iceland, *Quaternary Sci. Rev.*, 21, 2143–2177, [https://doi.org/10.1016/S0277-3791\(02\)00019-7](https://doi.org/10.1016/S0277-3791(02)00019-7), 2002.
- Evans, D. J. A., Phillips, E. R., Hiemstra, J. F., and Auton, C. A.: Subglacial till: formation, sedimentary characteristics and classification, *Earth-Sci. Rev.*, 78, 115–176, <https://doi.org/10.1016/j.earscirev.2006.04.001>, 2006.
- Eyles, N., Eyles, C. H., and Miall, A. D.: Lithofacies types and vertical profile models, an alternative approach to the description and environmental interpretation of glacial diamict and diamictite sequences, *Sedimentology*, 30, 393–410, <https://doi.org/10.1111/j.1365-3091.1983.tb00679.x>, 1983.
- Galbraith, R., Roberts, R., Laslett, G., Yoshida, H., and Olley, J.: Optical dating of single and multiple grains of Quartz from Jinmium rock shelter, northern Australia: Part I, experimental design and statistical models, *Archaeometry*, 41, 339–364, <https://doi.org/10.1111/j.1475-4754.1999.tb00987.x>, 1999.
- García, J.-L.: Late Pleistocene ice fluctuations and glacial geomorphology of the Archipiélago de Chiloé, southern Chile, *Geogr. Ann. A*, 94, 459–479, <https://doi.org/10.1111/j.1468-0459.2012.00471.x>, 2012.
- García, J.-L., Hein, A. S., Binnie, S. A., Gómez, G. A., González, M. A., and Dunai, T. J.: The MIS 3 maximum of the Torres del Paine and Última Esperanza ice lobes in Patagonia and the pacing of southern mountain glaciation, *Quaternary Sci. Rev.*, 185, 9–26, <https://doi.org/10.1016/j.quascirev.2018.01.013>, 2018.
- García, J.-L., Maldonado, A., de Porras, M. E., Nuevo Delaunay, A., Reyes, O., Ebensperger, C. A., Binnie, S. A., Lüthgens, C., and Méndez, C.: Early deglaciation and paleolake history of Río Cisnes Glacier, Patagonian Ice Sheet (44° S), *Quaternary Res.*, 91, 194–217, <https://doi.org/10.1017/qua.2018.93>, 2019.
- Garreaud, R. D.: Precipitation and circulation covariability in the extratropics, *J. Climate*, 20, 4789–4797, <https://doi.org/10.1175/JCLI4257.1>, 2007.
- Garreaud, R. D., Vuille, M., Compagnucci, R., and Marengo, J.: Present-day South America climate, *Palaeogeogr. Palaeoclimatol.*, 281, 180–195, <https://doi.org/10.1016/j.palaeo.2007.10.032>, 2009.
- Garreaud, R. D., Lopez, P., Minvielle, M., and Rojas, M.: Large-scale control on the Patagonian Climate, *J. Climate*, 26, 215–230, <https://doi.org/10.1175/JCLI-D-12-00001.1>, 2013.
- Glasser, N., Harrison, S., Ivy-Ochs, S., Duller, G., and Kubik, P.: Evidence from the Rio Bayo valley on the extent of the north Patagonian ice field during the late Pleistocene-Holocene transition, *Quaternary Res.*, 65, 70–77, <https://doi.org/10.1016/j.yqres.2005.09.002>, 2006.
- Harrison, S., Glasser, N., Winchester, V., Haresign, E., Warren, C., Duller, G., Bailey, R., Ivy-Ochs, S., Jansson, P., and Kubik, P.: Glaciar León, Chilean Patagonia: late-Holocene chronology and geomorphology, *Holocene*, 18, 643–652, <https://doi.org/10.1177/0959683607086771>, 2008.
- Hein, A. S.: Quaternary Glaciations in the Lago Pueyrredon Valley, Argentina, PhD thesis, The University of Edinburgh, Edinburgh, Scotland, 2009.

- Hein, A. S., Hulton, N. R. J., Dunai, T. J., Schnabel, C., Kaplan, M. R., Naylor, M., and Xu, S.: Middle Pleistocene glaciation in Patagonia dated by cosmogenic-nuclide measurements on outwash gravels, *Earth Planet. Sc. Lett.*, 286, 184–197, <https://doi.org/10.1016/j.epsl.2009.06.026>, 2009.
- Heusser, C. J. and Flint, R. F.: Quaternary glaciations and environments of northern Isla Grande de Chiloé, Chile, *Geology*, 5, 305–308, [https://doi.org/10.1130/0091-7613\(1977\)5<305:QGAEON>2.0.CO;2](https://doi.org/10.1130/0091-7613(1977)5<305:QGAEON>2.0.CO;2), 1977.
- Heusser, C. J., Lowell, T. V., Heusser, L. E., Hauser, A., Andersen, B. G., and Denton, G. H.: Full-glacial–late-glacial palaeoclimate of the Southern Andes: evidence from pollen, beetle, and glacial records, *J. Quaternary Sci.*, 11, 173–184, [https://doi.org/10.1002/\(SICI\)1099-1417\(199605/06\)11:3<173::AID-JQS237>3.0.CO;2-5](https://doi.org/10.1002/(SICI)1099-1417(199605/06)11:3<173::AID-JQS237>3.0.CO;2-5), 1996.
- Heusser, C. J., Heusser, L. E., and Lowell, T. V.: Paleoecology of the southern Chilean Lake District – Isla Grande de Chiloé during middle-Late Llanquihue glaciation and deglaciation, *Geogr. Ann. A*, 81, 231–284, <https://doi.org/10.1111/1468-0459.00058>, 1999.
- Hidy, A. J., Gosse, J. C., Pederson, J. L., Mattern, J. P., and Finkel, R. C.: A geologically constrained Monte Carlo approach to modeling exposure ages from profiles of cosmogenic nuclides: An example from Lees Ferry, Arizona, *Geochem. Geophys. Geosy.*, 11, Q0AA10, <https://doi.org/10.1029/2010GC003084>, 2010.
- Hogg, A. G., Hua, Q., Blackwell, P. G., Niu, M., Buck, C. E., Guilderson, T. P., Heaton, T. J., Palmer, J. G., Reimer, P. J., Reimer, R. W., Turney, C. S. M., and Zimmerman, S. R. H.: SHCal13 Southern Hemisphere Calibration, 0–50 000 Years cal BP, *Radiocarbon*, 55, 1889–1903, [https://doi.org/10.2458/azu\\_js\\_rc.55.16783](https://doi.org/10.2458/azu_js_rc.55.16783), 2013.
- Hubbard, A., Hein, A. S., Kaplan, M. R., Hulton, N. R. J., and Glasser, N.: A reconstruction of the late glacial maximum ice sheet and its deglaciation in the vicinity of the Northern Patagonian Icefield, South America, *Geogr. Ann. A*, 87, 375–391, <https://doi.org/10.1111/j.0435-3676.2005.00264.x>, 2005.
- Huntley, D. and Baril, M.: The K content of the K-feldspars being measured in optical and thermoluminescence dating, *Ancient TL*, 15, 11–13, 1997.
- Huntley, D. and Lamothe, M.: Ubiquity of anomalous fading in K-feldspars and the measurement and correction for it in optical dating, *Can. J. Earth Sci.*, 38, 1093–1106, <https://doi.org/10.1139/e01-013>, 2001.
- Ivy-Ochs, S., Kerschner, H., Reuther, A., Preusser, F., Heine, K., Maisch, M., Kubik, P. W., and Schlüchter, C.: Chronology of the last glacial cycle in the European Alps, *J. Quaternary Sci.*, 23, 559–573, <https://doi.org/10.1002/jqs.1202>, 2008.
- Jouzel, J., Masson-Delmotte, V., Cattani, O., Dreyfus, G., Falourd, S., Hoffmann, G., Minster, B., Nouet, J., Barnola, J. M., Chappellaz, J., Fischer, H., Gallet, J. C., Johnsen, S., Leuenberger, M., Loulergue, L., Luethi, D., Oerter, H., Parrenin, F., Raisbeck, G., Raynaud, D., Schilt, A., Schwander, J., Selmo, E., Souchez, R., Spahni, R., Stauffer, B., Steffensen, J. P., Stenni, B., Stocker, T. F., Tison, J. L., Werner, M., and Wolff, E. W.: Orbital and millennial Antarctic climate variability over the past 800 000 years, *Science*, 317, 793–796, <https://doi.org/10.1126/science.1141038>, 2007.
- Kaiser, J. and Lamy, F.: Links between Patagonian Ice Sheet fluctuations and Antarctic dust variability during the last glacial period (MIS 4–2), *Quaternary Sci. Rev.*, 29, 1464–1471, <https://doi.org/10.1016/j.quascirev.2010.03.005>, 2010.
- Kaiser, J., Lamy, F., and Hebbeln, D.: A 70 kyr sea surface temperature record off southern Chile (Ocean Drilling Program Site 1233), *Paleoceanography*, 20, PA4009, <https://doi.org/10.1029/2005PA001146>, 2005.
- Kaplan, M. R., Strelin, J. A., Schaefer, J. M., Denton, G. H., Finkel, R. C., Schwartz, R., Putnam, A. E., Vandergoes, M. J., Goehring, B. M., and Travis, S. G.: In-situ cosmogenic  $^{10}\text{Be}$  production rate at Lago Argentino, Patagonia: implications for late-glacial climate chronology, *Earth Planet. Sc. Lett.*, 309, 21–32, <https://doi.org/10.1016/j.epsl.2011.06.018>, 2011.
- Kelley, S. E., Kaplan, M. R., Schaefer, J. M., Andersen, B. G., Barrell, D. J. A., Putnam, A. E., Denton, G. H., Schwartz, R., Finkel, R. C., and Doughty, A. M.: High-precision  $^{10}\text{Be}$  chronology of moraines in the Southern Alps indicates synchronous cooling in Antarctica and New Zealand 42 000 years ago, *Earth Planet. Sc. Lett.*, 405, 194–206, <https://doi.org/10.1016/j.epsl.2014.07.031>, 2014.
- Kohl, C. P. and Nishiizumi, K.: Chemical isolation of quartz for measurement of *in-situ*-produced cosmogenic nuclides, *Geochim. Cosmochim. Ac.*, 56, 3583–3587, [https://doi.org/10.1016/0016-7037\(92\)90401-4](https://doi.org/10.1016/0016-7037(92)90401-4), 1992.
- Kreutzer, S., Schmidt, C., Fuchs, M., Dietze, M., and Fuchs, M.: Introducing an R package for luminescence dating analysis, *Ancient TL*, 30, 1–8, 2012.
- Kulig G.: Erstellung einer Auswertesoftware zur Altersbestimmung mittels Lumineszenzverfahren unter spezieller Berücksichtigung des Einflusses radioaktiver Ungleichgewichte in der  $^{238}\text{U}$ -Zerfallsreihe, B.Sc. thesis, Technische Universität Bergakademie, Freiberg, Germany, 35 pp., 2005.
- Lal, D.: Cosmic ray labeling of erosion surfaces: in-situ nuclide production rates and erosion models, *Earth Planet. Sc. Lett.*, 104, 424–439, [https://doi.org/10.1016/0012-821X\(91\)90220-C](https://doi.org/10.1016/0012-821X(91)90220-C), 1991.
- Lambert, F., Delmonte, B., Petit, J., Bigler, M., Kaufmann, P., Hutterli, M., Stocker, T., Ruth, U., Steffensen, J., and Maggi, V.: Dust-climate couplings over the past 800 000 years from the EPICA Dome C ice core, *Nature*, 452, 616–619, <https://doi.org/10.1038/nature06763>, 2008.
- Lamy, F., Kaiser, J., Ninnemann, U., Hebbeln, D., Arz, H. W., and Stoner, J.: Antarctic timing of surface water changes off Chile and Patagonian Ice Sheet response, *Science*, 304, 1959–1962, <https://doi.org/10.1126/science.1097863>, 2004.
- Lamy, F., Arz, H. W., Kilian, R., Lange, C. B., Lembke-Jene, L., Wengler, M., Kaiser, J., Baeza-Urrea, O., Hall, I. R., Harada, N., and Tiedemann, R.: Glacial reduction and millennial scale variations in Drake Passage throughflow, *P. Natl. Acad. Sci. USA*, 112, 13496–13501, <https://doi.org/10.1073/pnas.1509203112>, 2015.
- Laugénie, C.: La Région des Lacs, Chili Meridional, PhD diss., Université de Bordeaux, France, 1982.
- Lifton, N., Sato, T., and Dunai, T.: Scaling in situ cosmogenic nuclide production rates using analytical approximations to atmospheric cosmic-ray fluxes, *Earth Planet. Sc. Lett.*, 386, 149–160, <https://doi.org/10.1016/j.epsl.2013.10.052>, 2014.
- Lovejoy, S. and Lambert, F.: Spiky fluctuations and scaling in high-resolution EPICA ice core dust fluxes, *Clim. Past*, 15, 1999–2017, <https://doi.org/10.5194/cp-15-1999-2019>, 2019.



- Lowell, T. V., Heusser, C. J., Andersen, B. G., Moreno, P. I., Hauser, A., Heusser, L. E., Schlüchter, C., Marchant, D. R., and Denton, G. H.: Interhemispheric correlation of late Pleistocene glacial events, *Science*, 269, 1541–1549, <https://doi.org/10.1126/science.269.5230.1541>, 1995.
- Luebert, F. and Plissock, P.: Sinopsis bioclimática y vegetal de Chile, Editorial Universitaria, Santiago, Chile, ISBN 956-11-1832-7, 2006.
- Lüthgens, C., Neuhuber, S., Grupe, S., Payer, T., Peresson, M., and Fiebig, M.: Geochronological investigations using a combination of luminescence and cosmogenic nuclide burial dating of drill cores from the Vienna Basin, *Z. Dtsch. Ges. Geowiss.*, 168, 115–140, <https://doi.org/10.1127/zdgg/2017/0081>, 2017.
- Maizels, J.: Lithofacies variations within sandur deposits: the role of runoff regime, flow dynamics and sediment supply characteristics, *Sediment. Geol.*, 85, 299–325, [https://doi.org/10.1016/0037-0738\(93\)90090-R](https://doi.org/10.1016/0037-0738(93)90090-R), 1993.
- Manger, G. E.: Porosity and bulk density of sedimentary rocks, USGS Publications Warehouse, Washington D.C., Bulletin 1144-E, 55 pp., <https://doi.org/10.3133/b1144E>, 1963.
- Mayr, C., Stojakowits, P., Lempe, B., Blaauw, M., Diersche, V., Grohgan, M., López Correa, M., Ohlendorf, C., Reimer, P., and Zolitschka, B.: High-resolution geochemical record of environmental changes during MIS 3 from the northern Alps (Nesstetalgraben, Germany), *Quaternary Sci. Rev.*, 218, 122–136, <https://doi.org/10.1016/j.quascirev.2019.06.013>, 2019.
- Mejdahl, V.: Thermoluminescence dating: beta attenuation in quartz grains, *Achaeometry*, 21, 61–73, 1979.
- Mendelová, M., Hein, A. S., Rodés, A., and Xu, S.: Extensive mountain glaciation in central Patagonia during marine isotope stage 5, *Quaternary Sci. Rev.*, 227, 105996, <https://doi.org/10.1016/j.quascirev.2019.105996>, 2020.
- Menzies, J.: Strain pathways, till internal architecture and microstructures – perspectives on a general kinematic model – a “blueprint” for till development, *Quaternary Sci. Rev.*, 50, 105–124, <https://doi.org/10.1016/j.quascirev.2012.07.012>, 2012.
- Menzies, J., van der Meer, J. J. M., and Rose, J.: Till – as a glacial “tectonict”, its internal architecture, and the development of a “typing” method for till differentiation, *Geomorphology*, 75, 172–200, <https://doi.org/10.1016/j.geomorph.2004.02.017>, 2006.
- Mercer, J. H.: Chilean glacial chronology 20 000 to 11 000 carbon – 14 years ago: some global comparisons, *Science* 172, 1118–1120, <https://doi.org/10.1126/science.176.4039.1118>, 1972.
- Mercer, J. H.: Glacial history of southernmost South America, *Quaternary Res.*, 6, 125–166, [https://doi.org/10.1016/0033-5894\(76\)90047-8](https://doi.org/10.1016/0033-5894(76)90047-8), 1976.
- Miall, A. D.: Architectural-Element Analysis: A New Method of Facies Analysis Applied to Fluvial Deposits, *Earth-Sci. Rev.*, 22, 261–308, [https://doi.org/10.1016/0012-8252\(85\)90001-7](https://doi.org/10.1016/0012-8252(85)90001-7), 1985.
- Miall, A. D.: The Geology of Fluvial Deposits: Sedimentary facies, basin analysis and petroleum geology, Springer, Berlin, Germany, 582 pp., <https://doi.org/10.1007/978-3-662-03237-4>, 2006.
- Miller, J. H.: The climate of Chile, in: *Climates of Central and South America*, edited by: Schwerdtfeger, W., World Survey of Climatology, Elsevier, Amsterdam, The Netherlands, 113–145, 1976.
- NASA JPL: NASA Shuttle Radar Topography Mission Global 1 arc second, NASA EOSDIS Land Processes DAAC, USA, <https://doi.org/10.5067/MEaSURES/SRTM/SRTMGL1.003>, 2013.
- Nishiizumi, K., Imamura, M., Caffee, M. W., Southon, J. R., Finkel, R. C., and McAninch, J.: Absolute calibration of Be-10 AMS standards, *Nucl. Instrum. Meth. B*, 258, 403–413, <https://doi.org/10.1016/j.nimb.2007.01.297>, 2007.
- Parducci, L., Jorgensen, T., Tollefsrud, M. M., Elverland, E., Alm, T., Fontana, S. L., Bennett, K. D., Haile, J., Matetovici, I., Suyama, Y., Edwards, M. E., Andersen, K., Rasmussen, M., Boessenkool, S., Coissac, E., Brochmann, C., Taberlet, P., Houmark-Nielsen, M., Larsen, N. K., Orlando, L., Gilbert, M. T. P., Kjær, K. H., Greve, Alsos, I. G., and Willerslev, E.: Glacial survival of boreal trees in northern Scandinavia, *Science*, 335, 1083–1086, <https://doi.org/10.1126/science.1216043>, 2012.
- Parrenin, F., Masson-Delmotte, V., Koehler, P., Raynaud, D., Pailard, D., Schwander, J., Barbante, C., Landais, A., Wegner, A., and Jouzel, J.: Synchronous change of atmospheric CO<sub>2</sub> and Antarctic temperature during the last deglacial warming, *Science*, 339, 1060–1063, <https://doi.org/10.1126/science.1226368>, 2013.
- Porter, S.: Pleistocene Glaciations in the Southern Lake District of Chile, *Quaternary Res.*, 8, 2–31, [https://doi.org/10.1016/0033-5894\(81\)90013-2](https://doi.org/10.1016/0033-5894(81)90013-2), 1981.
- Prescott, J. and Hutton J.: Cosmic ray distributions to dose rates for luminescence and ESR dating: large depths and long-term variations, *Radiat. Meas.*, 23, 497–500, [https://doi.org/10.1016/1350-4487\(94\)90086-8](https://doi.org/10.1016/1350-4487(94)90086-8), 1994.
- Prescott, J. and Stephan, L.: The contribution of cosmic radiation to the environmental dose for thermoluminescent dating – Latitude, altitude and depth dependencies, *PACT. Revue du Groupe Européen d’Etudes pour les Techniques Physiques, Chimiques et Mathématiques Appliquées à l’Archéologie*, 6, 17–25, 1982.
- Preusser, F., Degering, D., Fuchs, M., Hilgers, A., Kadereit, A., Klasen, N., Krbetschek, M., Richter, D., and Spencer, J. Q. G.: Luminescence dating: basics, methods and applications, *E&G Quaternary Sci. J.*, 57, 95–149, <https://doi.org/10.3285/eg.57.1-2.5>, 2008.
- Putnam, A. E., Schaefer, J. M., Denton, G. H., Barrell, D. J. A., Birkel, S. D., Andersen, B. G., Kaplan, M. R., Finkel, R. C., Schwartz, R., and Doughty, A. M.: The Last Glacial Maximum at 44° S documented by a <sup>10</sup>Be moraine chronology at Lake Ohau, Southern Alps of New Zealand, *Quaternary Sci. Rev.*, 62, 114–141, <https://doi.org/10.1016/j.quascirev.2012.10.034>, 2013.
- Rhodes, E.: Optically Stimulated Luminescence Dating of Sediments over the Past 200 000, *Annu. Rev. Earth. Pl. Sc.*, 39, 461–488, <https://doi.org/10.1146/annurev-earth-040610-133425>, 2011.
- Rodés, Á., Pallàs, R., Braucher, R., Moreno, X., Masana, E., and Bourlés, D. L.: Effect of density uncertainties in cosmogenic <sup>10</sup>Be depth-profiles: dating a cemented Pleistocene alluvial fan (Carboneras Fault, SE Iberia), *Quat. Geochronol.*, 6, 186–194, <https://doi.org/10.1016/j.quageo.2010.10.004>, 2011.
- Roig, F. A., Le-Quesne, C., Boninsegna, J. A., Briffa, K. R., Lara, A., Grudd, H., Jones, P. D., and Villagrán, C.: Climate variability 50 000 years ago in mid-latitude Chile as reconstructed from tree rings, *Nature*, 410, 567–570, <https://doi.org/10.1038/35069040>, 2001.
- Sagredo, E. A., Moreno, P. I., Villa-Martinez, R., Kaplan, M. R., Kubik, P. W., and Stern, C. R.: Fluctuations of the Última Es-

- peranza ice lobe (52° S), Chilean Patagonia, during the last glacial maximum and termination 1, *Geomorphology*, 125, 92–108, <https://doi.org/10.1016/j.geomorph.2010.09.007>, 2011.
- Schaefer, J. M., Putnam, A. E., Denton, G. H., Kaplan, M. R., Birkel, S., Ninneman, U. S., Barker, S., Schwartz, R., Andersen, B. J., and Schluechter, C.: The southern glacial maximum 65 000 years ago and its unfinished termination, *Quaternary Sci. Rev.*, 114, 52–60, <https://doi.org/10.1016/j.quascirev.2015.02.009>, 2015.
- Shackleton, N. J., Hall, M. A., and Vincent, E.: Phase relationships between millennial-scale events 64 000–24 000 years ago, *Paleoceanography*, 15, 565–569, <https://doi.org/10.1029/2000PA000513>, 2000.
- Shulmeister, J., Thackray, G. D., Rieser, U., Hyatt, O. M., Rother, H., Smart, C. C., and Evans, D. J.: The stratigraphy, timing and climatic implications of glaciolacustrine deposits in the middle Rakaia Valley, South Island, New Zealand, *Quaternary Sci. Rev.*, 29, 2362–2381, <https://doi.org/10.1016/j.quascirev.2010.06.004>, 2010.
- Smedley, R. K., Glasser, N. F., and Duller, G. A. T.: Luminescence dating of glacial advances at Lago Buenos Aires (~46° S), Patagonia, *Quaternary Sci. Rev.*, 134, 59–73, <https://doi.org/10.1016/j.quascirev.2015.12.010>, 2016.
- Strub, P. T., Mesias, J. M., Montecino, V., Ruttant, J., and Salinas, S.: Coastal ocean circulation off western South America, in: *The Global Coastal Ocean: Regional Studies and Synthesis*, edited by: Robinson, A. R. and Brink K. H., John Wiley, New York, USA, 273–315, 1998.
- Stuiver, M., Reimer, P. J., and Reimer, R. W.: CALIB 7.1 [WWW program], available at: <http://calib.org>, last access: 16 April 2020.
- Sugden, D. E., McCulloch, R. D., Bory, A. J.-M., and Hein, A. S.: Influence of Patagonian glaciers on Antarctic dust deposition during the last glacial period, *Nat. Geosci.*, 2, 281–285, <https://doi.org/10.1038/ngeo474>, 2009.
- Villagrán, C.: Expansion of Magellanic moorland during the Late Pleistocene: palynological evidence from northern Isla Grande de Chiloé, *Quaternary Res.*, 30, 304–314, [https://doi.org/10.1016/0033-5894\(88\)90006-3](https://doi.org/10.1016/0033-5894(88)90006-3), 1988.
- Villagrán, C.: Glacial, Late-Glacial, and Post-Glacial climate and vegetation of the Isla Grande de Chiloé, Southern Chile (41–44° S), *Quat. S. Am. A.*, 8, 1–15, 1990.
- Villagrán, C., León, A., and Roig, F. A.: Paleodistribución del alerce y ciprés de las Guaitecas durante períodos interestadiales de la Glaciación Llanquihue: provincias de Llanquihue y Chiloé, Región de Los Lagos, Chile, *Rev. Geol. Chile*, 31, 133–151, <https://doi.org/10.4067/S0716-02082004000100008>, 2004.
- Villagrán, C., Abarzúa, A. M., and Armesto, J.: Nuevas evidencias paleobotánicas y filogeográficas en torno a la historia Cuaternaria de los bosques subtropical-templados de la Cordillera de la Costa de Chile, in: *Biodiversidad y Ecología de los bosques costeros de Chile*, edited by: Smith-Ramirez, C. and Squeo, F., Editorial Universidad de Los Lagos, Chile, 3–21, 2019.
- WAIS Divide Project Members: Precise interpolar phasing of abrupt climate change during the last ice age, *Nature*, 520, 661–665, <https://doi.org/10.1038/nature14401>, 2015.
- Williams, P. W., McGlone, M., Neil, H., and Zhao, J.-X.: A review of New Zealand palaeoclimate from the last interglacial to the global last glacial maximum, *Quaternary Sci. Rev.*, 110, 92–106, <https://doi.org/10.1016/j.quascirev.2014.12.017>, 2015.
- Wintle, A.: Anomalous Fading of Thermo-luminescence in Mineral Samples, *Nature*, 245, 143–144, <https://doi.org/10.1038/245143a0>, 1973.
- Wintle, A.: Luminescence dating: where it has been and where it is going, *Boreas*, 37, 471–482, <https://doi.org/10.1111/j.1502-3885.2008.00059.x>, 2008.